FISEVIER

Contents lists available at ScienceDirect

## Journal of Fluids and Structures

journal homepage: www.elsevier.com/locate/jfs



# A frequency-domain flutter solver for rotary-wing aeroelasticity

David Quero

DLR (German Aerospace Center), Institute of Aeroelasticity, Göttingen 37073, Germany

### ARTICLE INFO

Keywords:
Aeroelasticity
Fluid-structure interaction
Flutter solver
Rotary-wing
Floquet theory

### ABSTRACT

A frequency-domain flutter solver for rotary-wing aeroelasticity is presented. The method applies to linear time-periodic (LTP) aeroelastic systems, including helicopters in forward flight, propellers with yaw angle, and wind energy turbines. It assumes a frequency-domain representation of the aerodynamic model, using the aerodynamic harmonic transfer function (HTF), denoted here as the harmonic generalized aerodynamic force (GAF) matrix. This accounts for the effects of harmonics of the fundamental or forcing frequency. The harmonic GAF exhibits a nonlinear dependence on the Laplace variable, and after coupling with the structural model, the relevant subset of Floquet exponents is determined by solving a nonlinear eigenvalue problem.

This method extends the conventional flutter solvers used in fixed-wing aeroelasticity, which are based on a linear time-invariant (LTI) system. Specifically, it introduces harmonic extensions of the p-k and g flutter solvers, termed the h-p-k and h-g solvers, making them applicable to rotary-wing aeroelasticity. When applied to an LTI system, the method naturally reduces to the standard p-k and g flutter solvers used in fixed-wing aeroelasticity.

The proposed method is demonstrated on a two-degree-of-freedom rotor blade section in forward flight, incorporating an unsteady aerodynamic model based on potential flow theory. It accurately predicts the same advance ratio for flutter onset as the Floquet method while eliminating the need to construct the monodromy matrix. Furthermore, it enables stability analysis even when the aerodynamic model is not available in state-space form, allowing for the use of nonparametric aerodynamic representations.

### 1. Introduction

A key concern in rotorcraft aeroelastic response is the risk of instabilities, which can arise both on the ground and in flight. In flight, helicopter rotor blades operate in a highly complex aeroelastic environment where aerodynamic forces and blade vibrations interact, potentially leading to flutter instability. Unlike fixed-wing flutter, rotor blade flutter in forward flight occurs under time-periodic conditions due to rotation and forward motion. At high forward speeds, the advancing blade experiences transonic flow, while the retreating blade undergoes flow reversal and dynamic stall, resulting in a highly nonlinear aerodynamic environment. Ensuring stability under these conditions is critical for flight safety and has been a central focus of rotorcraft research for decades.

A primary goal in rotorcraft aeroelasticity is to reduce development risks associated with advanced rotorcraft designs, enabling engineers to integrate new technologies while mitigating the risk of unforeseen instabilities. Without an effective aeroelastic stability analysis framework, designers may be forced to adopt overly conservative approaches, leading to lower performance designs or necessitating extensive testing, both of which significantly impact cost and development schedules. Moreover, encountering unexpected instabilities during flight testing can severely disrupt development timelines, drive cost overruns, or even jeopardize entire programs.

E-mail address: David.QueroMartin@dlr.de.

https://doi.org/10.1016/j.jfluidstructs.2025.104435

Received 11 March 2025; Received in revised form 17 July 2025; Accepted 29 September 2025

Available online 4 October 2025

0889-9746/© 2025 The Author. Published by Elsevier Ltd. This is an open access article under the CC BY license (http://creativecommons.org/licenses/by/4.0/).

A gap of nearly four decades exists between the evolution of fixed-wing and rotary-wing aeroelastic technologies (Friedmann, 2004). Some aerodynamic challenges specific to rotary-wing aircraft, particularly those related to unsteady flow phenomena, remain poorly understood. Nonetheless, research in rotary-wing aeroelasticity has been active in recent decades, aiming to address these challenges.

Ormiston et al. (1988) conducted a comprehensive review of rotorcraft aeroelastic stability research, emphasizing the field's complexity and scope. Before 1970, several experimental compound helicopters extended rotorcraft flight testing to high-speed, high-advance ratio values, revealing stability issues at these conditions. Early studies predominantly focused on bending-torsion rotor blade flutter, including wake-induced instabilities. At the time, unsteady aerodynamic theories for rotor-blade flutter were largely based on two-dimensional models such as Theodorsen and Loewy theories. Following 1970, the introduction of Floquet theory enabled researchers to address the longstanding challenge of forward-flight aeroelastic stability. Concurrently, aerodynamic modeling was expanded to incorporate three-dimensional effects, dynamic inflow for low-frequency aeroelastic stability, transonic tip aerodynamics, and dynamic stall. Ormiston et al. (1988) stated that frequency-domain formulations are not well suited for rotary-wing aeroelastic stability analysis in forward flight due to the periodic nature of rotor systems. This study addresses this limitation by developing a frequency-domain flutter solver to effectively analyze rotor stability in forward flight conditions.

In fixed-wing aeroelasticity, the dominant instability mechanism is coupled bending-torsion flutter, whereas in rotary-wing aeroelasticity, it is the coupled flap-lag-torsion response of an isolated blade. Rotary-wing aeroelastic instabilities can be classified into two primary flight regimes: hover and forward flight. In hover, the governing equations of motion exhibit constant coefficients, while in forward flight, the coefficients become periodic due to the blade's rotation and changing aerodynamic conditions. Stability boundaries are typically determined by linearizing the equations of motion about the equilibrium position derived from a coupled trim-aeroelastic analysis. Eigenanalysis is used to assess stability in hover, while forward-flight stability is typically analyzed using Floquet theory (Floquet, 1883; Lowis, 1963; Peters and Hohenemser, 1971; Friedmann et al., 1977; Peters and Su, 1990). This involves perturbing the nonlinear blade motion equations around a periodic forced response and evaluating damping characteristics using Floquet eigenanalysis (Friedmann, 1986; Gaonkar and Peters, 1980).

Lowis (1963) examined a rigid rotor blade with a flapping hinge under quasi-steady aerodynamic conditions, demonstrating that increasing advance ratios in forward flight lead to greater destabilization regions. Crimi (1969) conducted aeroelastic stability analysis of helicopter rotors using quasi-steady aerodynamics, highlighting key differences between rotor flutter in hover and forward flight. While hover flutter resembles classical fixed-wing flutter formulations, forward-flight flutter is inherently different due to the periodic nature of aerodynamic forces acting on the blade as it rotates. Consequently, the rotor's equations of motion contain periodically varying coefficients. Crimi (1973) later extended this analysis by incorporating a two-dimensional airfoil undergoing dynamic stall, coupled with an elastomechanical model that included flapping, flapwise bending, and torsional degrees of freedom, revealing instabilities analogous to both classical flutter and stall flutter in forward flight.

Panda and Chopra (1985) explored the aeroelastic stability of a three-degree-of-freedom (flap-lag-torsion) rotor blade in forward flight, utilizing quasi-steady aerodynamics with a dynamic inflow model. They solved the periodic perturbation equations using both Floquet theory and a constant coefficient approximation in the fixed reference frame, demonstrating that a time-averaged coefficient approximation is valid only for lower forward speeds (advance ratios  $\mu$  < 0.2). Dinyavari (1985) and Dinyavari and Friedmann (1986) modeled forward-flight equations of motion as nonlinear differential equations with periodic coefficients. Their approach involved evaluating the helicopter's trim state, linearizing the equations about the nonlinear periodic equilibrium, and determining stability using Floquet theory by computing characteristic exponents (Friedmann et al., 1977). Dinyavari and Friedmann also integrated finite-state time-domain aerodynamics into rotary-wing aeroelastic models for both hover and forward flight, enabling coupled nonlinear flap-lag analysis. Due to the periodic coefficients in forward-flight dynamic equations, frequency-domain unsteady aerodynamic theories are generally inadequate, prompting many studies to rely on quasi-steady aerodynamics (Dinyavari and Friedmann, 1986). This work, however, aims to develop a frequency-domain flutter solver specifically tailored for linear time-periodic (LTP) aeroelastic systems.

The aerodynamic environment surrounding helicopter rotors in forward flight is inherently complex and highly unsteady. Below the stall regime, free-wake analysis and lifting-surface theories are commonly used to model blade/vortex interactions and three-dimensional tip effects. However, the interplay between blade advancing motion and rotational speed creates multiple flow regimes, including transonic shock waves on the advancing blade, flow reversal, and unsteady stall on the retreating blade. As a result, capturing nonlinear transonic effects at the blade tip requires high-fidelity computational fluid dynamics (CFD) simulations. Additionally, the periodic nature of the rotor wake further complicates the aerodynamic loading, significantly impacting aeroelastic stability boundaries (Dinyavari, 1985; Dinyavari and Friedmann, 1986; Torok and Chopra, 1990).

Torok and Chopra (1990) emphasized that research on rotor aeroelastic stability in forward flight remains limited due to the intricacy of the aerodynamic environment, which involves dynamic stall, flow separation, and transonic effects. For a comprehensive assessment of rotor stability, the aerodynamic model must be sufficiently sophisticated to account for a wide range of flight conditions, from attached flow to dynamically stalled compressible flow.

Floquet theory has long been regarded as the most effective tool for analyzing the stability of systems governed by linearized equations with periodic coefficients. The method, initially applied by Lowis (1963) and later expanded by Peters and Hohenemser (1971), requires time-marching integration of the dynamic equations over a full period and subsequent eigenanalysis of the transition matrix to determine stability. Recent research has focused on incorporating sophisticated aerodynamic models with implicit states that cannot be directly perturbed, leading to various truncation methods to approximate stability solutions. However, as Peters and Su (1990) emphasized, hidden aerodynamic states can significantly influence blade dynamics and should not be constrained during perturbation-based Floquet analysis.

Bauchau and Wang (2010) applied their algorithms to a complete aeroelastic system, incorporating the coupling between structural and aerodynamic models. This approach underscored the importance of selecting suitable excitations that adequately energize the modes of interest, particularly the least damped ones. In contrast, the method presented in this work determines the stability of all modes by solving the associated nonlinear eigenvalue problem, explicitly separating structural and aerodynamic models, similar to the *p-k* (Hassig, 1971) and *g* (Chen, 2000) flutter solvers used in fixed-wing aeroelasticity. Additionally, partial Floquet theory is inherently a time-domain method since it relies on an approximated monodromy matrix. Skjoldan and Bauchau (2011) further applied partial Floquet analysis to wind energy turbines.

Yeo et al. (2011) conducted a rotor aeroelastic stability analysis on a hingeless rotor in hover and forward flight using a high-fidelity aeroelastic model. They employed direct time-domain numerical integration of the governing equations in response to a targeted excitation, utilizing a tightly coupled computational fluid dynamics (CFD) and computational structural dynamics (CSM) framework. The free-decay transient response time histories were postprocessed using the moving-block method to determine damping variations with rotor operating conditions. Their results closely aligned with experimental data, outperforming conventional aerodynamic methods and underscoring the significance of accurate aerodynamic modeling in rotor aeroelastic stability predictions. However, their analysis did not account for the impact of the perturbation timing on the time-periodic system. The present work seeks a frequency-domain approach to enable a more efficient aeroelastic stability assessment, eliminating the need for repeated CFD-CSM simulations for different aerodynamic models.

Zaki (2012) applied perturbation loads at the three-quarter span location of the UH-60 A rotor blade and utilized four signals to construct the required Hankel matrices. These signals included flap and lag displacements, the lag rotation angle at the blade's three-quarter span, and the root flap angle. In stable systems, accurately evaluating damping levels in the least damped modes is crucial, as these values depend on all forces acting on the rotor. Therefore, obtaining precise aerodynamic load estimates is essential for reliable damping predictions.

None of the previous works have applied a frequency-domain approach (commonly used in fixed-wing aeroelasticity) to rotary-wing aeroelastic problems involving periodic conditions. Instead, they rely on either computing the monodromy matrix using Floquet theory or truncating it with partial Floquet theory. To the best of the author's knowledge, this work is the first to introduce an alternative approach by developing a frequency-domain flutter solver that explicitly separates structural and aerodynamic models, similar to the p-k and g methods used in fixed-wing aeroelasticity. By employing the concept of the harmonic transfer function for the aerodynamic system, a nonlinear aerodynamic model (regardless of its complexity) can be incorporated in a straightforward manner. Leveraging a frequency-domain approach, this study aims to provide a computationally efficient method for analyzing rotorcraft aeroelastic stability in forward flight conditions.

Although primarily motivated by rotor blade stability analysis in forward flight, this work focuses on the general derivation of the flutter solution method itself. As a result, the approach can potentially be applied to any aeroelastic linear time-periodic (LTP) system, including propellers in yaw conditions or wind energy turbines.

Section 2 introduces a brief overview of LTP system theory, followed by its frequency-domain representation using the harmonic transfer function in Section 3. The frequency-domain flutter solver is presented in Section 4, where the h-p-k and h-g flutter solution method (natural extensions of the p-k and g methods from fixed-wing aeroelasticity) are derived for rotary-wing applications. Section 5 presents a forward-flight application to a helicopter rotor blade, employing a potential-flow model for the unsteady aerodynamics. Section 6 presents the conclusions.

### 2. Linear time-periodic systems

The review provided here is based on the work of Wereley (1991). A generic linear time-periodic (LTP) system in continuous time can be expressed in state-space form as:

$$\frac{d\mathbf{x}(t)}{dt} = \mathbf{A}(t)\mathbf{x}(t) + \mathbf{B}(t)\mathbf{u}(t), \tag{1}$$

$$\mathbf{y}(t) = \mathbf{C}(t)\mathbf{x}(t) + \mathbf{D}(t)\mathbf{u}(t). \tag{2}$$

where  $\mathbf{x}(t) \in \mathbb{R}^{n_s}$  represents the state vector and  $\mathbf{y}(t) \in \mathbb{R}^{n_y}$  the output vector. The state-space matrices  $\mathbf{A}(t) \in \mathbb{R}^{n_s \times n_s}$ ,  $\mathbf{B}(t) \in \mathbb{R}^{n_s \times n_u}$ ,  $\mathbf{C}(t) \in \mathbb{R}^{n_y \times n_s}$  and  $\mathbf{D}(t) \in \mathbb{R}^{n_y \times n_u}$  exhibit periodicity with period  $T = 2\pi/\omega_0$ :

$$\mathbf{A}(t) = \mathbf{A}(t+T), \ \mathbf{B}(t) = \mathbf{B}(t+T),$$
 (3)

$$\mathbf{C}(t) = \mathbf{C}(t+T), \ \mathbf{D}(t) = \mathbf{D}(t+T),$$
(4)

To analyze the stability of this LTP system, the corresponding autonomous system is considered together with initial conditions  $\mathbf{x}_0$ :

$$\frac{d\mathbf{x}(t)}{dt} = \mathbf{A}(t)\mathbf{x}(t), \ \mathbf{x}(0) = \mathbf{x}_0.$$

### 2.1. Floquet theory

Now, consider the homogeneous LTP system with period T, described by

$$\frac{d\mathbf{x}\left(t\right)}{dt} = \mathbf{A}\left(t\right)\mathbf{x}\left(t\right),\tag{5}$$

where  $\mathbf{x} \in \mathbb{R}^{n_s}$  and  $\mathbf{A} \in \mathbb{R}^{n_s \times n_s}$  satisfies the periodicity condition:  $\mathbf{A}(t+T) = \mathbf{A}(t)$ . A fundamental or transition matrix solution, denoted by  $\psi(t,t_0)$ , consists of a fundamental set of independent solutions arranged in columns and satisfies:

$$\frac{d\boldsymbol{\psi}\left(t,t_{0}\right)}{dt} = \mathbf{A}\left(t\right)\boldsymbol{\psi}\left(t,t_{0}\right),\tag{6}$$

with appropriate initial conditions  $\psi(t_0)$ . Setting the initial condition as  $\psi(t_0) = \mathbf{I}$  defines the principal fundamental matrix  $\phi(t,t_0)$ , from which any fundamental matrix can be obtained as  $\phi(t,t_0) = \psi(t,t_0) \psi^{-1}(t_0)$ . The solution to the system described in Eq. (5) can then be expressed as  $\mathbf{x}(t) = \phi(t,t_0) \mathbf{x}_0$ . Since the principal fundamental matrix  $\phi(t,t_0)$  satisfies Eq. (6), evaluating it at t+T gives:

$$\frac{d\boldsymbol{\phi}\left(t+T,t_{0}\right)}{dt}=\mathbf{A}\left(t+T\right)\boldsymbol{\phi}\left(t+T,t_{0}\right)=\mathbf{A}\left(t\right)\boldsymbol{\phi}\left(t+T,t_{0}\right),\tag{7}$$

which implies that  $\phi(t+T,t_0)$  must be a linear combination of  $\phi(t,t_0)$ , since both satisfy the same state equation:

$$\boldsymbol{\phi}(t+T,t_0) = \boldsymbol{\phi}(t,t_0)\,\boldsymbol{\beta} = \boldsymbol{\phi}(t,t_0)\,\boldsymbol{\beta}^{\mathrm{RT}},\tag{8}$$

or equivalently:

$$\beta = e^{\mathbf{R}T} = \phi^{-1}(t, t_0) \phi(t + T, t_0). \tag{9}$$

Floquet theory establishes that the state transition matrix  $\phi(t+T,t_0)$  can be decomposed as

$$\phi(t,t_0) = \mathbf{P}(t) e^{\mathbf{R}(t-t_0)} \mathbf{P}^{-1}(t_0), \tag{10}$$

where  $\mathbf{P}(t) \in \mathbb{C}^{n_s \times n_s}$  is a T-periodic complex matrix. With the additional condition that  $\mathbf{P}(0) = \mathbf{I}$ , the solution of the homogeneous LTP system consists of an exponential factor multiplied by a purely periodic matrix  $\mathbf{P}(t)$ ,  $\mathbf{x}(t) = \boldsymbol{\phi}(t,0)\mathbf{x}_0 = \mathbf{P}(t)e^{\mathbf{R}t}\mathbf{x}_0$ . Since  $\mathbf{P}(T) = \mathbf{P}(0) = \mathbf{I}$ , evaluating Eq. (9) at  $t = t_0 = 0$  yields the monodromy matrix  $\boldsymbol{\phi}(T)$ :

$$\phi(T) = \beta = e^{\mathbf{R}T}$$
.

From Eq. (8) follows that  $\phi(t + NT, t_0) = \phi(t, t_0) \beta^N$ . Now, considering the eigenvalue decomposition of the monodromy matrix  $\phi(T)$ :

$$\phi(T) = \text{Sdiag}\left(\rho_1, \dots, \rho_{n_s}\right) \mathbf{S}^{-1},$$

it follows that  $\phi^N(T) = \operatorname{Sdiag}\left(\rho_1^N, \dots, \rho_{n_s}^N\right) \mathbf{S}^{-1}$ . The system is unstable if any eigenvalue  $\rho_j$  satisfies  $\left|\rho_j\right| > 1$  for  $j = 1, \dots, n_s$ . From the definition of the monodromy matrix  $\phi(T) = e^{\mathbf{R}T}$  it follows that the eigenvalues  $\rho_j$  of  $\phi(T)$  are related to the eigenvalues  $\mu_j$  of the matrix  $\mathbf{R}$  by:

$$e^{\mu_j T} = \rho_j, \quad j = 1, \dots, n_s.$$

Solving for  $\mu_i$  gives:

$$\mu_j = \frac{\ln\left(\rho_j\right)}{T} + il\omega_0, \quad j = 1, \dots, n_s, \quad l \in \mathbb{Z},\tag{11}$$

where  $\omega_0 = 2\pi/T$  is the fundamental frequency, and l is an arbitrary integer. The system is unstable if any eigenvalue of  $\mathbf{R}$  has a positive real part, Re  $(\mu_j) > 0$  for any  $j = 1, \dots, n_s$ . Eq. (11) shows that for each state component j, an infinite number of Floquet exponents  $\mu_j$  contribute to the system response (Bottasso and Cacciola, 2015). However, all exponents differ by integer multiples of  $\omega_0$  while sharing the same real part, meaning that each mode is either entirely stable or unstable. The exponents are folded within the fundamental strip, which contains the imaginary axis in the range  $\omega \in (-\omega_0/2, -\omega_0/2]$  (Wereley, 1991). This is expected, as the stability of the system is determined solely by the characteristic multipliers, which are uniquely defined.

Since all Floquet exponents  $\mu_j$  for a given j share the same real part, tracking one exponent per mode suffices to determine the stability of the LTP aeroelastic system. In essence, the Floquet exponents  $\mu_j$  play a role analogous to eigenvalues in the LTI case, defining mode frequencies through their imaginary part and damping characteristics through their real part.

While this work focuses on Floquet exponents, it its worth noting that interpreting the associated periodic eigenvectors defined by P(t) may provide further insight into the LTP system (Bottasso and Cacciola, 2015). Floquet eigenvectors contain all integer-multiple frequencies and remain a unique contribution regardless of the choice of the integer l (Peters and Lieb, 2009). These eigenvectors capture the true frequency content of system dynamics, including the relative strengths of each harmonic multiple. However, since stability is determined solely by the real part of the Floquet exponents, this work does not pursue an analysis of periodic eigenvectors.

Numerical computation of the monodromy matrix

Since no explicit general expression for the monodromy matrix  $\phi(T)$  is known for LTP systems, its determination relies on the numerical integration of the system defined by Eq. (5), with appropriate initial conditions (Peters and Hohenemser, 1971). This requires solving  $n_s$  independent simulations, each initialized with  $\mathbf{x}_{0,j} = \mathbf{e}_j$ , where  $\mathbf{e}_j$  is a unit a vector with all zeros except for a one in position j. Consequently, as the number of states  $n_s$  increases, the computational cost grows significantly. This is not only due to the increased size of the system but also because a larger number of simulations must be performed. Methods such as the partial Floquet analysis attempt to mitigate this issue, but as discussed in Section 1, no automated approach exists for generating the required set of dynamic simulations, making engineering judgment necessary.

The numerical integration of the homogeneous Eq. (5) is crucial for determining the Floquet exponents  $\mu_j$  and, thus, system stability. In particular, the choice of time step size or the maximum error allowed in a variable time-stepping algorithm must be carefully considered. The sensitivity of the Floquet exponents to numerical precision in computing the monodromy matrix  $\phi(T)$  has been demonstrated in Maurice et al. (2009) for a helicopter in forward flight.

When computing Floquet exponents from the eigenvalues of the monodromy matrix, additional effort is required compared to LTI systems, as the exponents may include integer-multiple harmonics, as indicated by Eq. (11). On the other hand, as described in Section 3.1, the Hill determinant method serves as a frequency-domain counterpart to Floquet theory for stability analysis. However, this approach further complicates eigenvalue sorting due to the presence of spurious poles, which arise from the truncation necessary for a finite representation of the Hill matrix. In contrast, the frequency-domain flutter solver proposed in this work (Section 4) inherently resolves the sorting and tracking of relevant aeroelastic eigenvalues, eliminating these challenges and simplifying the stability analysis process.

### 2.2. Time-invariant average system

As noted by Maurice et al. (2009), using an LTI-averaged does not yield reliable conclusions regarding system stability. In the constant coefficient approximation, periodic terms are averaged over the period, effectively retaining only the zero Fourier series coefficient. Stability is then evaluated by solving an eigenvalue problem. Biggers (1974) investigated the stability of rotor blades in forward flight using the constant-coefficient approximation. This approach involves first applying a multiblade coordinate (MBC) transformation to convert the system into a non-rotating coordinate frame, where some of the periodic effects due to forward flight are transformed into constant terms. By time-averaging the remaining periodic terms, Biggers concluded that this approximation is suitable for analyzing the flapping stability of rotor blades at advance ratios up to 0.5, particularly for the lower-frequency modes. Gaonkar and Peters (1980) extended the MBC transformation for automated application and demonstrated that the constant-coefficient approximation in multiblade coordinates remains satisfactory for flap-lag stability analyses, including rotor-body coupling with dynamic inflow, for advance ratios up to 0.4. Bir (2008) provides a detailed explanation of the MBC transformation, along with a clear summary of the associated assumptions. Skjoldan and Hansen (2009) generalized the concept of isotropy for wind turbines to account for aerodynamic and control effects, thereby broadening the applicability of the Coleman transformation. Although this transformation is a powerful and practical tool for simple, low-dimensional models, it becomes impractical when applied to large-scale multiphysics models coupled with CFD simulations or experimental data.

Further applications of this approach can be found in Panda and Chopra (1985) for helicopter blades and Stol et al. (2009) for wind turbines. For the interested reader, Maggia et al. (2020) present a detailed method for generating higher-order averaging terms to better approximate the original LTP system. To demonstrate the importance of periodic terms and justify the flutter solver developed in this work for the application case in Section 5, the averaging method is applied to the system in its original rotating coordinates, as the averaging process itself is not the primary focus here. Although applying an MBC transformation could enhance stability predictions, the LTI-averaged method is unlikely to provide accurate results for the advance ratios above 0.5 considered in Section 5, regardless of whether MBC is used.

### 3. Frequency-domain representation

To determine the stability of the LTP aeroelastic system, the aerodynamic system is considered separately from the structural model. This approach is also employed in frequency-domain solvers for fixed-wing aeroelasticity, such as the p-k and g methods. Typically, the generalized coordinates representing the structural modes, contained in the matrix  $\phi_{gh}$ , serve as inputs to the aerodynamic system, while the generalized aerodynamic forces (GAF) are already projected onto the structural modes.

Wereley (1991) introduced an approach by transforming input and output signals of LTP systems to exponentially modulated periodic (EMP) signals, defined as:

$$\mathbf{u}(t) = e^{st} \sum_{n \in \mathbb{Z}} \mathbf{u}_n e^{in\omega_0 t} = \sum_{n \in \mathbb{Z}} \mathbf{u}_n e^{s_n t} \approx \sum_{n = -n_H}^{n_H} \mathbf{u}_n e^{s_n t}, \quad s_n = s + in\omega_0,$$

$$(12)$$

where s is in general complex,  $s \in \mathbb{C}$ . The EMP signal results from the product of a complex exponential  $e^{st}$  with a periodic function expanded in a Fourier series.

If the state-space matrices from Eqs. (1) and (2) are known, the so-called harmonic transfer function (HTF), which relates inputs and outputs in EMP form, can be computed. Assuming an EMP input as in Eq. (12), the state  $\mathbf{x}(t)$  and the output  $\mathbf{y}(t)$  also take an EMP form (Wereley, 1991):

$$\mathbf{x}\left(t\right) = \sum_{n \in \mathbb{Z}} \mathbf{x}_{n} e^{s_{n}t}, \ \mathbf{y}\left(t\right) = \sum_{n \in \mathbb{Z}} \mathbf{y}_{n} e^{s_{n}t}.$$

The derivative of the state is then given by:

$$\frac{d\mathbf{x}\left(t\right)}{dt}=\sum_{n\in\mathbb{Z}}s_{n}\mathbf{x}_{n}e^{s_{n}t}.$$

For a Fourier series decomposition of the periodic state-space matrices:

$$\mathbf{A}\left(t\right) = \sum_{n \in \mathbb{Z}} \mathbf{A}_{n} e^{in\omega_{0}t}, \ \mathbf{B}\left(t\right) = \sum_{n \in \mathbb{Z}} \mathbf{B}_{n} e^{in\omega_{0}t}, \ \mathbf{C}\left(t\right) = \sum_{n \in \mathbb{Z}} \mathbf{C}_{n} e^{in\omega_{0}t}, \ \mathbf{D}\left(t\right) = \sum_{n \in \mathbb{Z}} \mathbf{D}_{n} e^{in\omega_{0}t},$$

substituting these expressions in Eqs. (1) and (2) yields:

$$\sum_{n \in \mathbb{Z}} s_n \mathbf{x}_n e^{s_n t} = \left(\sum_{n \in \mathbb{Z}} \mathbf{A}_n e^{in\omega_0 t}\right) \left(\sum_{n \in \mathbb{Z}} \mathbf{x}_n e^{s_n t}\right) + \left(\sum_{n \in \mathbb{Z}} \mathbf{B}_n e^{in\omega_0 t}\right) \left(\sum_{n \in \mathbb{Z}} \mathbf{u}_n e^{s_n t}\right) \\
= \sum_{n, m \in \mathbb{Z}} \mathbf{A}_{n-m} \mathbf{x}_m e^{s_n t} + \sum_{n, m \in \mathbb{Z}} \mathbf{B}_{n-m} \mathbf{u}_m e^{s_n t},$$
(13)

for the state equation, and

$$\sum_{n\in\mathbb{Z}} \mathbf{y}_n e^{s_n t} = \sum_{n,m\in\mathbb{Z}} \mathbf{C}_{n-m} \mathbf{x}_m e^{s_n t} + \sum_{n,m\in\mathbb{Z}} \mathbf{D}_{n-m} \mathbf{u}_m e^{s_n t}, \tag{14}$$

for the output equation.

Applying a harmonic balance procedure, that is, equating the coefficients for each harmonic n, leads to:

$$s_n \mathbf{x}_n = \sum_{m \in \mathbb{Z}} \mathbf{A}_{n-m} \mathbf{x}_m + \sum_{m \in \mathbb{Z}} \mathbf{B}_{n-m} \mathbf{u}_m, \tag{15}$$

$$\mathbf{y}_n = \sum_{m \in \mathbb{Z}} \mathbf{C}_{n-m} \mathbf{x}_m + \sum_{m \in \mathbb{Z}} \mathbf{D}_{n-m} \mathbf{u}_m. \tag{16}$$
 These equations can be rewritten as a doubly infinite matrix equation:

$$s\mathcal{X}(s) = (A - \mathcal{N})\mathcal{X}(s) + B\mathcal{U}(s), \tag{17}$$

$$\mathcal{Y}(s) = \mathcal{CX}(s) + \mathcal{DV}(s), \tag{18}$$

where the doubly infinite vectors are:

$$\mathcal{U}\left(s\right) = \begin{bmatrix} \cdots & \mathbf{u}_{-1}^T & \mathbf{u}_0^T & \mathbf{u}_1^T & \ldots \end{bmatrix}^T, \ \mathcal{Y}\left(s\right) = \begin{bmatrix} \cdots & \mathbf{y}_{-1}^T & \mathbf{y}_0^T & \mathbf{y}_1^T & \ldots \end{bmatrix}^T, \ \mathcal{X}\left(s\right) = \begin{bmatrix} \cdots & \mathbf{x}_{-1}^T & \mathbf{x}_0^T & \mathbf{x}_1^T & \ldots \end{bmatrix}^T.$$

The doubly infinite Toeplitz matrices are defined as:

$$\mathcal{A} = \begin{bmatrix}
\ddots & \vdots & & & \vdots \\
\cdots & \mathbf{A}_{0} & \mathbf{A}_{-1} & \mathbf{A}_{-2} & \mathbf{A}_{-3} & \cdots \\
& \mathbf{A}_{1} & \mathbf{A}_{0} & \mathbf{A}_{-1} & \mathbf{A}_{-2} \\
& \mathbf{A}_{2} & \mathbf{A}_{1} & \mathbf{A}_{0} & \mathbf{A}_{-1} \\
\cdots & \mathbf{A}_{3} & \mathbf{A}_{2} & \mathbf{A}_{1} & \mathbf{A}_{0} & \cdots \\
\vdots & & \vdots & \ddots
\end{bmatrix},$$
(19)

and similarly for  $\mathcal{B}$ ,  $\mathcal{C}$  and  $\mathcal{D}$ . The modulation frequency matrix  $\mathcal{N}$  is:

$$\mathcal{N} = \begin{bmatrix}
\ddots & \vdots & & \vdots \\
\cdots & -i\omega_0 \mathbf{I}_{n_s} & \mathbf{0} & \mathbf{0} \\
& \mathbf{0} & \mathbf{0} & \mathbf{0} \\
\cdots & \mathbf{0} & 0 & i\omega_0 \mathbf{I}_{n_s} & \cdots \\
\vdots & \vdots & \ddots
\end{bmatrix}$$
(20)

From Eqs. (17) and (18), the harmonic transfer function (HTF) matrix  $\mathcal{H}(s)$  is defined as:

$$\mathcal{Y}(s) = \mathcal{H}(s) \, \mathcal{U}(s), \tag{21}$$

where:

$$\mathcal{H}(s) = C \left[ s\mathbf{I} - (A - \mathcal{N}) \right]^{-1} \mathcal{B} + \mathcal{D}, \tag{22}$$

The HTF matrix has a doubly infinite dimensional structure (Möllerstedt, 2000; Bittanti and Colaneri, 2009):

$$\mathcal{H}(s) = \begin{bmatrix} \ddots & \vdots & & \vdots \\ \cdots & \mathbf{H}_{0} \left( s - i\omega_{0} \right) & \mathbf{H}_{-1} \left( s \right) & \mathbf{H}_{-2} \left( s + i\omega_{0} \right) & \cdots \\ & \mathbf{H}_{1} \left( s - i\omega_{0} \right) & \mathbf{H}_{0} \left( s \right) & \mathbf{H}_{-1} \left( s + i\omega_{0} \right) \\ \cdots & \mathbf{H}_{2} \left( s - i\omega_{0} \right) & \mathbf{H}_{1} \left( s \right) & \mathbf{H}_{0} \left( s + i\omega_{0} \right) & \cdots \\ \vdots & \vdots & \ddots \end{bmatrix}$$

$$(23)$$

For practical numerical computations, truncation must be applied to the HTF matrix  $\mathcal{H}(s)$  by limiting the number of harmonics to  $n_H$ . The integer index n ranges from  $-n_H$  to  $n_H$ , resulting in a total of  $2n_H+1$  terms in the Fourier series expansion (for periodic statespace matrices) or EMP series expansion (for the input, output and state vectors). However, even after truncation to  $n_H$  harmonics, the HTF matrix still includes terms ranging from  $-2n_H$  to  $2n_H$ , as seen in Eq. (23).

A useful property for numerical applications is the symmetry property of the HTF (Möllerstedt, 2000):

$$\mathbf{H}_{n}(s) = \tilde{\mathbf{H}}_{-n}(\bar{s}), \tag{24}$$

where - denotes the complex conjugate.

#### 3.1. Hill determinant

To determine the stability of the LTP system using the Hill determinant formulation, consider the unforced state-space model:

$$\frac{d\mathbf{x}\left(t\right)}{dt} = \mathbf{A}\left(t\right)\mathbf{x}\left(t\right).$$

Applying the harmonic balance procedure as described in Section 3, the following equation is obtained:

$$s_n \mathbf{x}_n - \sum_{n=0}^{\infty} \mathbf{A}_{n-m} \mathbf{x}_m = \mathbf{0}.$$

Considering all harmonics, the infinite set of equations can be expressed in matrix form as:

$$\left[\mathcal{I} - \left(s\mathcal{I} + \mathcal{N}\right)^{-1} \mathcal{A}\right] \mathcal{X} = \mathbf{0},\tag{25}$$

where  $\mathcal{I}$  represents the doubly infinite identity matrix, and the matrices  $\mathcal{A}$  and  $\mathcal{N}$  have been previously defined in Eqs. (19) and (20). Eq. (25) has a nontrivial solution if the infinite determinant equals zero:

$$\det\left(\mathcal{I} - \left(s\mathcal{I} + \mathcal{N}\right)^{-1}\mathcal{A}\right) = 0. \tag{26}$$

The real part of s will determine the stability of the system, as it indicates whether the signals grow or decay after each period. When computing the Floquet exponents using the Hill determinant method, truncation of the involved Fourier series can affect accuracy. Some eigenvalues align more closely with the central rows of the Toeplitz matrix A, making them less sensitive to truncation and providing a better approximation of the Floquet exponents (Lazarus and Thomas, 2010). Applying the Hill method without additional considerations may lead to incorrect stability predictions due to the presence of spurious Floquet exponents that have no physical meaning. Therefore, when using the Hill method, a subset of the computed Floquet exponents must be selected to discard non-physical ones.

Some selection criteria are based on the most symmetric eigenvectors, as proposed by Lazarus and Thomas (Lazarus and Thomas, 2010), since they have shown faster convergence to the actual Floquet exponents, even though no formal proof of convergence exists for the symmetry-based sorting method.

### 3.2. Frequency-domain identification of the harmonic transfer function

This section addresses the identification of the harmonic transfer function (HTF) in the frequency domain using simulated data. For a more detailed discussion, the reader is referred to Siddiqi (2001) and Hidir et al. (2019). Siddiqi obtained the HTF using chirp signals applied at specific times within the period, while Hidir et al. used multicosine signals covering a range of frequencies. The work of Allen (2009) is also noteworthy, though it focuses on identifying the state matrix without considering external inputs, which are required for this study.

In contrast, this work proposes a more direct approach, extracting the Fourier coefficients of the system function matrix  $\mathbf{H}(\omega, t)$ directly from simulated data. In Section 3, the HTF matrix, which relates EMP input signals to EMP output signals, was introduced. Here, a direct connection is established with the Fourier series coefficients of the system function matrix  $\mathbf{H}(\omega, t)$ . This matrix defines the output  $\mathbf{y}(t)$  in response to an input of the form  $\mathbf{u}(t) = e^{i\omega t}\mathbf{u}_0$  as (Zadeh, 1950):

$$\mathbf{y}(t) = e^{i\omega t} \mathbf{H}(\omega, t) \mathbf{u}_0. \tag{27}$$

When applied to the EMP input signal from Eq. (12) with  $2n_H$  harmonics and setting  $s = i\omega$ , this results in:

$$\mathbf{y}(t) = e^{i\omega t} \sum_{n=-2n_H}^{2n_H} \mathbf{H}\left(\omega + n\omega_0, t\right) \mathbf{u}_n e^{in\omega_0 t}.$$
Approximating  $\mathbf{H}\left(\omega + n\omega_0, t\right)$  with a truncated Fourier series of  $2n_H$  harmonics:

$$\mathbf{y}\left(t\right)=e^{i\omega t}\left(\sum_{n=-n_{H}}^{2n_{H}}\sum_{m=-n_{H}}^{2n_{H}}\hat{\mathbf{H}}_{m}\left(\omega+n\omega_{0}\right)\mathbf{u}_{n}\right)e^{i(n+m)\omega_{0}t},$$

which is equivalent to:

$$\mathbf{y}(t) = e^{i\omega t} \sum_{m = -4n_H}^{4n_H} \left( \sum_{n = \max(-2n_H, m - 2n_H)}^{\min(2n_H, m + 2n_H)} \hat{\mathbf{H}}_{m - n} \left( \omega + n\omega_0 \right) \mathbf{u}_n \right) e^{im\omega_0 t}.$$
(29)

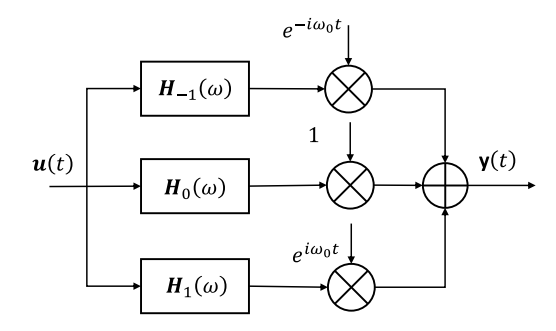


Fig. 1. Time-domain representation of an LTP system.

By retaining  $n_H$  harmonics in Eq. (29), the output y(t) can be expressed as:

$$\mathbf{y}(t) \approx e^{i\omega t} \sum_{m=-n_H}^{n_H} \mathbf{y}_m e^{im\omega_0 t},$$

where:

$$\mathbf{y}_{m} = \sum_{n=-n_{H}}^{n_{H}} \hat{\mathbf{H}}_{m-n} \left( \omega + n\omega_{0} \right) \mathbf{u}_{n}, \quad n = 1, \dots, n_{H}.$$

The corresponding Fourier coefficients  $\mathbf{y}_m(\omega)$  for  $m=-n_H,\ldots,n_H$ , which depend on the excitation frequency  $\omega$ , can be assembled in matrix form as:

$$\begin{bmatrix} \mathbf{y}_{-n_{H}}(\omega) \\ \vdots \\ \mathbf{y}_{0}(\omega) \\ \vdots \\ \mathbf{y}_{n_{H}}(\omega) \end{bmatrix} = \begin{bmatrix} \hat{\mathbf{H}}_{0}(\omega - n_{H}\omega_{0}) & \cdots & \hat{\mathbf{H}}_{-n_{H}}(\omega) & \cdots & \hat{\mathbf{H}}_{-2n_{H}}(\omega + n_{H}\omega_{0}) \\ \vdots & \ddots & & \vdots \\ \hat{\mathbf{H}}_{n_{H}}(\omega - n_{H}\omega_{0}) & \cdots & \hat{\mathbf{H}}_{0}(\omega) & \cdots & \hat{\mathbf{H}}_{-n_{H}}(\omega + n_{H}\omega_{0}) \\ \vdots & & \ddots & & \vdots \\ \hat{\mathbf{H}}_{2n_{H}}(\omega - n_{H}\omega_{0}) & \cdots & \hat{\mathbf{H}}_{n_{H}}(\omega) & \cdots & \hat{\mathbf{H}}_{0}(\omega + n_{H}\omega_{0}) \end{bmatrix} \begin{bmatrix} \mathbf{u}_{-n_{H}}(\omega) \\ \vdots \\ \mathbf{u}_{0}(\omega) \\ \vdots \\ \mathbf{u}_{n_{H}}(\omega) \end{bmatrix}.$$

$$(30)$$

This can be rewritten compactly as:

$$\mathcal{Y}(\omega) = \mathcal{H}(\omega) \mathcal{U}(\omega)$$
. (31)

The truncated version of the HTF matrix  $\mathcal{H}(s)$ , evaluated at the imaginary axis  $(s = j\omega)$ , can thus be constructed directly from the Fourier series coefficients  $\hat{\mathbf{H}}_n$  of the system function matrix  $\mathbf{H}(\omega,t)$ , evaluated at specific frequency shifts of  $\omega$ . For an inputoutput representation with  $n_H$  harmonics, the HTF matrix includes terms ranging from  $\hat{\mathbf{H}}_{-2n_H}$  to  $\hat{\mathbf{H}}_{2n_H}$ , explaining the choice of  $2n_H$  harmonics in Eq. (28).

Möllerstedt (2000) discussed in chapter 5 the effect of truncation on the HTF matrix and established two conditions that must be met for truncation to be valid; (1) The system gain must be low for high input frequencies, and (2) the high-frequency output must be small.

In this work, these conditions are assumed to hold, and truncation is shown to provide excellent results for the application case in Section 5.

Fig. 1 illustrates the time-domain output  $\mathbf{y}(t)$  in response to an arbitrary input  $\mathbf{u}(t)$ , obtained using the following convolution relation (Möllerstedt, 2000; Bittanti and Colaneri, 2009):

$$\mathbf{y}(t) = \sum_{n=-n_H}^{n_H} \left( \hat{\mathbf{h}}_n(t) * \mathbf{u}(t) \right) e^{in\omega_0 t}, \tag{32}$$

where \* denotes the convolution operator, and  $\hat{\mathbf{h}}_n(t)$  corresponding to the Fourier coefficients of the modified impulse response matrix. These coefficients can be obtained as the inverse Fourier transform of the Fourier coefficients of the system function matrix  $\hat{\mathbf{H}}_n(\omega)$  (Quero, 2024). For clarity, only one harmonic ( $n_H = 1$ ) is shown.

An equivalent frequency-domain representation is shown in Fig. 2 and can be written as follows (Bittanti and Colaneri, 2009; Hidir et al., 2019):

$$\mathbf{y}\left(\omega\right) = \sum_{n=-n_{H}}^{n_{H}} \hat{\mathbf{H}}_{n}\left(\omega\right) \mathbf{u}\left(\omega + n\omega_{0}t\right),$$

where the associated HTF terms correspond to those in the middle column of the HTF matrix provided in Eq. (30) (see Fig. 2).

Similar to the transfer function matrix in the LTI case, different methods can be used to compute the HTF matrix of an LTP system:

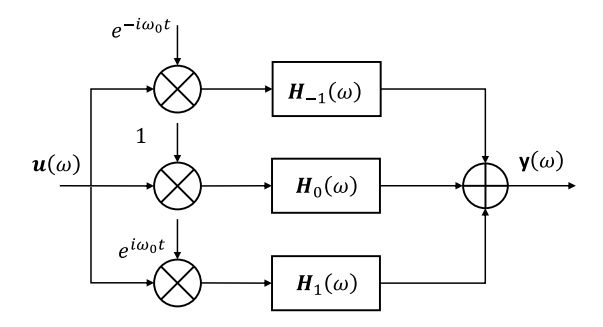


Fig. 2. Frequency-domain representation of an LTP system.

- Direct computation of the HTF matrix. Proposed by Wereley (1991), this method is well-suited for EMP signals. Quero (2024) further showed that the harmonic linear frequency-domain (HLFD) method, which is closely related to HTF computation, can be used to determine the system response to an arbitrary input signal.
- Identification using pulse responses in the time domain. This method, introduced by Quero (2024), involves identifying the HTF matrix from a set of pulse responses. As in the LTI case, these signals excite a wide frequency band in each simulation.
- Frequency-domain techniques using chirp signals as described by Siddiqi (2001) and Hidir et al. (2019), this approach involves using chirp signals to estimate the HTF matrix.
- Identification using sine and cosine signals. This method, proposed by Hidir et al. (2019) and applied with slight modifications
  in this work, involves exciting the system with sinusoidal inputs at various excitation frequencies. The procedure is detailed
  next.

Identification using sine and cosine input signals

To obtain the system function matrix  $\mathbf{H}(\omega, t)$  from simulated responses, both cosine and sine functions are applied as inputs:

$$\mathbf{u}_{m,c}(t,\omega) = u_c(t,\omega)\mathbf{e}_m, \ u_c(t,\omega) = u_0\cos(\omega t), \ m=1,\ldots,n_u$$

$$\mathbf{u}_{m,s}(t,\omega) = u_s(t,\omega)\,\mathbf{e}_m, \ u_c(t,\omega) = u_0\sin(\omega t), \ m = 1,\dots,n_u.$$

For an HTF resolution of  $n_H$  harmonics, twice this number is required in the system function matrix  $\mathbf{H}(\omega,t)$ . For numerical implementation, a frequency interval is selected with  $n_{\omega}$  different values for  $\omega$  in the frequency range of interest. Due to the symmetry property of Eq. (24), only positive values of  $\omega$  are considered, as the negative frequencies can be obtained as  $\mathbf{H}_n(-\omega) = \bar{\mathbf{H}}_{-n}(\omega)$ .

By simulating multiple periods to allow transient effects to decay, the system function matrix  $\mathbf{H}(\omega, t)$  can be determined at a given frequency  $\omega$  using Eq. (27):

$$\mathbf{H}(\omega,t)\mathbf{e}_{m} = \left(\mathbf{y}_{m,c}(t,\omega) + i\mathbf{y}_{m,s}(t,\omega)\right)e^{-i\omega t},\tag{33}$$

where  $\mathbf{y}_{m,c}(t,\tau_k)$  is the output to the cosine input  $\mathbf{u}_{m,c}(t,\omega)$ , and  $\mathbf{y}_{m,s}(t,\omega)$  is the output to the sine input  $\mathbf{u}_{m,s}(t,\omega)$ . Applying a Fourier series expansion with  $2n_H$  harmonics, the system function matrix can be expressed as:

$$\mathbf{H}\left(\omega,t\right)=\sum_{n=-2n_{H}}^{2n_{H}}\hat{\mathbf{H}}_{n}\left(\omega\right)e^{in\omega_{0}t},\label{eq:Hamiltonian}$$

where the Fourier coefficients are given by:

$$\hat{\mathbf{H}}_{n}(\omega) = \frac{1}{T} \int_{0}^{T} \mathbf{H}(\omega, t) e^{-in\omega_{0}t} dt.$$

The obtained set of Fourier series  $\hat{\mathbf{H}}_n(\omega)$  form the middle column of the truncated HTF matrix  $\mathcal{H}(\omega)$  in Eq. (31). The remaining columns can be obtained by interpolation at the requested frequency values  $\omega + n\omega_0$  for  $n = n_H, \dots, n_H$ .

Figs. 3 and 4 illustrate the response of the first output component to a cosine and sine input signals at  $\omega=10$  (rad/s) for a system with fundamental frequency  $\omega_0=22.82$  (rad/s), using an input applied at component m=2 (see Section 5). For an LTI system the system function matrix  $\mathbf{H}(\omega,t)$  obtained from both the cosine and sine responses (using Eq. (33)) is simply a complex number. However, for an LTP system, it is a periodic signal, which can be represented as a truncated Fourier series. By expressing  $(\mathbf{y}_{m,c}(t,\omega)+i\mathbf{y}_{m,s}(t,\omega))\,e^{-i\omega t}$  as a truncated Fourier series, number of harmonics  $n_H$  required for an accurate representation can be directly estimated. Once  $n_H$  is determined, twice this number must be considered to construct the HTF matrix in Eq. (31).

### 4. Frequency-domain flutter solver

This section presents a novel flutter solver formulated entirely in the frequency domain, applicable to rotary-wing aeroelasticity. The method applies to LTP aeroelastic systems and reduces to the LTI formulation of fixed-wing aeroelasticity as a special case.

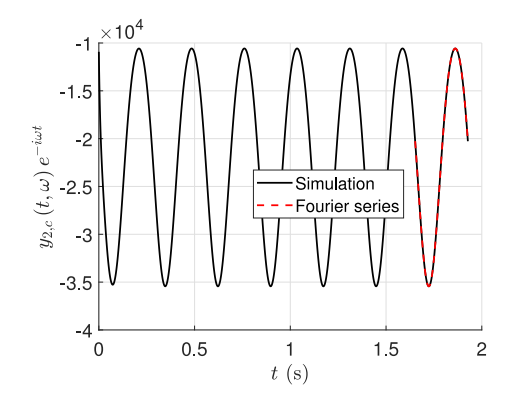


Fig. 3. Signal  $y_{m,c}(t,\omega)e^{-i\omega t}$  from a response to a cosine signal at frequency  $\omega=10$  (rad/s), along with its Fourier series approximation using two harmonics.

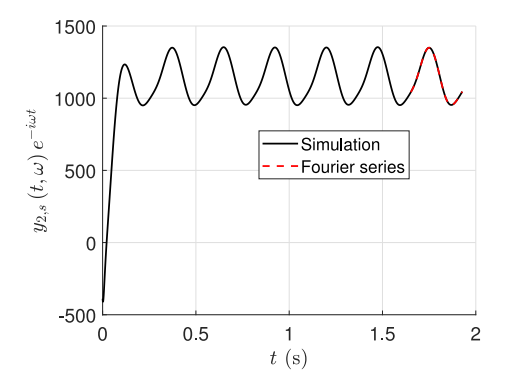


Fig. 4. Signal  $y_{m,s}(t,\omega) e^{-i\omega t}$  from a response to a sine signal at frequency  $\omega = 10$  (rad/s), along with its Fourier series approximation using two harmonics.

In this work, the trim problem is neglected, and a nominal periodic equilibrium condition is assumed, around which stability is analyzed. The physical coordinates  $\mathbf{u}_g$  contain deviations from this equilibrium. The aeroelastic system can be described in the time domain by:

$$\mathbf{M}_{gg}\left(\omega_{0}\right)\frac{d^{2}\mathbf{u}_{g}}{dt^{2}}+\mathbf{B}_{gg}\left(\omega_{0}\right)\frac{d\mathbf{u}_{g}}{dt}+\mathbf{K}_{gg}\left(\omega_{0}\right)\mathbf{u}_{g}=\mathbf{F}_{a}\left[\mathbf{u}_{g},\frac{d\mathbf{u}_{g}}{dt},\frac{d^{2}\mathbf{u}_{g}}{dt^{2}}\right]\left(t,M_{\infty},Re_{\infty},\omega_{0},\mu\right),$$

with  $\mathbf{u}_g$  the physical coordinates,  $\mathbf{M}_{gg}$ ,  $\mathbf{B}_{gg}$  and  $\mathbf{K}_{gg}$  the mass, damping, and stiffness matrices respectively, and  $\mathbf{F}_a$  represents the time-dependent aerodynamic operator including possible additional forces. The rotating coordinate system is assumed, so that a single independent blade is considered and the structural matrices already include the required gyroscopic, Coriolis and centrifugal forces with fundamental frequency  $\omega_0$  determined by the rotor speed. Additional blade control effects, such as pitch-flap kinematic coupling, can be incorporated directly into the structural matrices (Johnson, 2012). In Section 5, the structural matrices are considered constant and independent of  $\omega_0$ , but the proposed method applies to cases where they depend on the rotor speed. Additionally, the structural matrices are considered time-invariant. If they exhibit time dependence, a similar HTF analysis, as applied to the aerodynamic system, can be extended to the structural matrices.

By projecting of the physical coordinates  $\mathbf{u}_g$  with the matrix including the wind-off structural modes ( $\phi_{gh}$ ), the governing equation transforms into:

$$\mathbf{M}_{hh}\left(\omega_{0}\right)\frac{d^{2}\mathbf{u}_{h}}{dt^{2}}+\mathbf{B}_{hh}\left(\omega_{0}\right)\frac{d\mathbf{u}_{h}}{dt}+\mathbf{K}_{hh}\left(\omega_{0}\right)\mathbf{u}_{h}=\mathbf{F}_{h}\left[\mathbf{u}_{h},\frac{d\mathbf{u}_{h}}{dt},\frac{d^{2}\mathbf{u}_{h}}{dt^{2}}\right]\left(t,M_{\infty},Re_{\infty},\omega_{0},\mu\right).$$
(34)

Here, the generalized structural mass, damping and stiffness matrices are given by:

$$\mathbf{M}_{hh} = \boldsymbol{\phi}_{gh}^T \mathbf{M}_{gg} \boldsymbol{\phi}_{gh}, \ \mathbf{B}_{hh} = \boldsymbol{\phi}_{gh}^T \mathbf{B}_{gg} \boldsymbol{\phi}_{gh}, \ \mathbf{K}_{hh} = \boldsymbol{\phi}_{gh}^T \mathbf{K}_{gg} \boldsymbol{\phi}_{gh},$$

and the aerodynamic (and possibly additional external) forces  $\mathbf{F}_h = \boldsymbol{\phi}_{gh}^T \mathbf{F}_a$  have been projected onto the structural modes. For systems with a high number of physical degrees of freedom (DOF), the number of structural modes  $\boldsymbol{\phi}_{gh}$  can be truncated, reducing the size of  $\mathbf{u}_h$  while retaining relevant modes. Examples of structural mode extraction for rotating beams can be found in the works of Houbolt and Brooks (1958) for torsional modes, as well as Myklestad (1944) and Prohl (1945) for uncoupled bending modes.

The aerodynamic forces in Eq. (34) depend explicitly on  $\omega_0$  and the advance ratio  $\mu$  for helicopter rotor blades. However, in the case of propellers or wind turbines, this dependency may also arise due to the yaw angle. Additionally, compressibility and viscosity effects are represented by the Mach number  $(M_{\infty})$  and Reynolds number  $(Re_{\infty})$ , respectively. The aerodynamic term also depends on the periodic equilibrium conditions, though this dependence is not explicitly stated for clarity. Due to the time-periodic nature of the aerodynamic forces, the overall aeroelastic system exhibits LTP behavior.

By applying an EMP input signal as in Eq. (12):

$$\mathbf{u}_h = e^{st} \sum_{n \in \mathbb{Z}} \mathbf{u}_{h,n} e^{in\omega_0 t} = \sum_{n \in \mathbb{Z}} \mathbf{u}_{h,n} e^{(s+in\omega_0)t}.$$
Its first- and second-time derivatives are:

$$\frac{d\mathbf{u}_h}{dt} = \left(s + in\omega_0\right) \sum_{n \in \mathbb{Z}} \mathbf{u}_{h,n} e^{\left(s + in\omega_0\right)t}, \quad \frac{d^2\mathbf{u}_h}{dt^2} = \left(s + in\omega_0\right)^2 \sum_{n \in \mathbb{Z}} \mathbf{u}_{h,n} e^{\left(s + in\omega_0\right)t}.$$
The aerodynamic forces can be expressed in terms of the HTF matrix:

$$\mathcal{F}_{h}(s) = \mathcal{Q}_{hh}\left(p, M_{\infty}, \omega_{0}, \mu\right) \mathcal{U}_{h}(s), \tag{37}$$

where  $Q_{hh}(p, M_{\infty}, \omega_0, \mu)$  represents the aerodynamic HTF matrix, a natural extension of the generalized aerodynamic forces (GAF) used in fixed-wing aeroelasticity (Hassig, 1971; Chen, 2000; Quero et al., 2021). This double-infinite matrix, referred to here as the harmonic GAF matrix, represents the application of Eq. (21) to the aerodynamic system under consideration. For clarity, explicit dependence on the Reynolds number  $Re_{\infty}$  has been omitted.

Substituting Eqs. (35)-(37) into Eq. (34), and equating the coefficients corresponding to each harmonic component n:

$$\left[\left(s+in\omega_{0}\right)^{2}\mathbf{M}_{hh}\left(\omega_{0}\right)+\left(s+in\omega_{0}\right)\mathbf{B}_{hh}\left(\omega_{0}\right)+\mathbf{K}_{hh}\left(\omega_{0}\right)\right]\mathbf{u}_{h,n}=\mathbf{F}_{h,n}=\mathbf{T}_{n}\mathcal{Q}_{hh}\left(s,M_{\infty},\omega_{0},\mu\right)\mathcal{U}_{h}\left(s\right).$$

Here, the matrix  $\mathbf{T}_n$  selects the appropriate rows from the infinite vector  $\mathcal{U}_h$  corresponding to the harmonic component n. Stacking all harmonics together, and introducing the nondimensional Laplace variable  $p = g + ik = sL_{ref}/U_{\infty}$ , the following infinite set of matrix equations is obtained:

$$\left(\left(p\left(\frac{U_{\infty}}{L_{ref}}\right)\mathcal{I}+i\omega_{0}\mathcal{N}\right)^{2}\otimes\mathbf{M}_{hh}\left(\omega_{0}\right)+\left(p\left(\frac{U_{\infty}}{L_{ref}}\right)\mathcal{I}+i\omega_{0}\mathcal{N}\right)\otimes\mathbf{B}_{hh}\left(\omega_{0}\right)+\mathcal{I}\otimes\mathbf{K}_{hh}\left(\omega_{0}\right)-\mathcal{Q}_{hh}\left(p,M_{\infty},\omega_{0},\mu\right)\right)\mathcal{V}_{h}\left(p\right)=\mathbf{0},$$
(38)

where:

$$\mathcal{N} = \begin{bmatrix} \ddots & \vdots & & \vdots \\ \cdots & -1 & 0 & 0 \\ & 0 & 0 & 0 \\ \cdots & 0 & 0 & 1 & \cdots \\ & \vdots & & \vdots & \ddots \end{bmatrix}, \ \mathcal{I} = \begin{bmatrix} \ddots & \vdots & & \vdots \\ \cdots & 1 & 0 & 0 \\ & 0 & 1 & 0 \\ \cdots & 0 & 0 & 1 & \cdots \\ & \vdots & & \vdots & \ddots \end{bmatrix}.$$
 To enable practical computation, the number of harmonics in  $\mathcal{U}_h(p)$  is truncated to  $n_H$ . The system in Eq. (38) is then rewritten

$$\left[ \left( p \left( \frac{U_{\infty}}{L_{ref}} \right) \mathbf{I}_{(2n_{H}+1)} + i\omega_{0} \mathbf{N} \right)^{2} \otimes \mathbf{M}_{hh} \left( \omega_{0} \right) + \left( p \left( \frac{U_{\infty}}{L_{ref}} \right) \mathbf{I}_{(2n_{H}+1)} + i\omega_{0} \mathbf{N} \right) \otimes \mathbf{B}_{hh} \left( \omega_{0} \right) \right. \\
+ \left. \left( \mathbf{I}_{2n_{H}+1} \otimes \mathbf{K}_{hh} \left( \omega_{0} \right) \right) - \mathcal{Q}_{hh} \left( p, M_{\infty}, \omega_{0}, \mu \right) \right] \mathcal{U}_{h} \left( p \right) = \mathbf{0}, \tag{39}$$

where:

$$N = diag(-n_H, \dots, n_H)$$
.

Eq. (39) represents the novel flutter equation formulated in the frequency domain, as proposed in this work. Its solution determines the complex Floquet exponents,  $\mu$ , which appear in the exponential term  $e^{st}$  with  $s = \mu$ , when  $\mathbf{u}_h$  is an EMP signal, as described in Eq. (35). As discussed in Section 2.1, the stability of the LTP system is governed by the sign of the real part of the Floquet exponents.

Unlike the truncation of the monodromy matrix used by Torok and Chopra (1990), the method proposed here explicitly accounts for the influence of aerodynamic forces on the structure. By choosing an appropriate initial value for the nonlinear eigenvalue solver, the subset related to structural modes can be identified, similar to the approach in fixed-wing aeroelasticity when using frequency-domain solvers like the p-k or g methods.

The harmonic GAF matrix,  $Q_{hh}(p, M_{\infty}, \omega_0, \mu)$ , generally exhibits a nonlinear dependence on the Laplace variable p, as is also the case in fixed-wing aeroelasticity (Hassig, 1971; Quero et al., 2021). Consequently, similar approximations used in the LTI case for fixed-wing aeroelasticity are applied here. Specifically, the harmonic GAF matrix can be approximated by its values along the imaginary axis:

$$Q_{hh}(p, M_{\infty}, \omega_0, \mu) \approx Q_{hh}(ik, M_{\infty}, \omega_0, \mu). \tag{40}$$

By combining Eq. (39) with the approximation in Eq. (40), the so-called h-p-k flutter solution method is derived, which extends the commonly used p-k method (Hassig, 1971) from fixed-wing to rotary-wing aeroelasticity. The h-p-k method reduces to the p-k method in the time-invariant case, that is, when  $n_H = 0$ . Inspired by the g method (Chen, 2000), an additional extension is formulated using the following approximation:

$$Q_{hh}\left(p,M_{\infty},\omega_{0},\mu\right)\approx Q_{hh}\left(ik,M_{\infty},\omega_{0},\mu\right)+g\frac{dQ_{hh}\left(ik,M_{\infty},\omega_{0},\mu\right)}{d\left(ik\right)}\tag{41}$$

By incorporating Eq. (41) into Eq. (39), the h-g method is established, an extension of the g flutter solution method to rotary-wing aeroelasticity. Similar to the h-p-k method, the h-g method reduces to the g method when  $n_H = 0$ . The aerodynamic GAF over the imaginary axis can then be determined using various methods described in Section 3.2.

A key advantage of the proposed flutter solution method is its ability to utilize a non-parametric representation of the aerodynamic system, requiring only the harmonic GAF matrix without necessitating a state-space structure. This provides an alternative to the Floquet or Hill methods (Sections 2.1 and 3.1), where a state-space representation is required. This feature is particularly beneficial when extracting the harmonic GAF matrix from high-fidelity simulations or experimental data.

For solving the nonlinear algebraic Eq. (39), a dedicated nonlinear solver is employed (Quero et al., 2021). To maintain a consistent number of equations and unknowns, one component of the associated (truncated) eigenvector  $\mathcal{U}_h(p)$  is fixed. Analogous to the p-k or g methods in fixed-wing aeroelasticity, proper initialization is essential. The hover condition ( $\mu$  = 0) is selected as the starting point. By incrementally increasing the advance ratio  $\mu$  and using the previous aeroelastic mode's eigensolution as the initial condition, the evolution of damping and frequency of the Floquet exponents can be effectively tracked.

For LTP systems, an infinite number of Floquet exponents exist, shifted by integer multiples of the fundamental frequency  $\omega_0$ . This introduces ambiguity when tracking eigensolutions, though only the real part of each infinite set is relevant for stability determination. As noted by Skjoldan and Bauchau (2011), integer multiples of the rotor speed can be added to the principal frequencies to obtain more physically meaningful results. The proposed flutter solution method resolves this ambiguity by tracking eigensolutions from the hover case, ensuring meaningful eigenvalues. While additional Floquet exponents shifted by integer multiples of the fundamental frequency may contribute to specific initial conditions, only one exponent per aeroelastic mode is necessary for stability analysis, as all share the same real part.

In summary, the proposed flutter solver offers several advantages over existing methods for stability analysis of LTP aeroelastic systems:

- Automatic elimination of spurious poles. Unlike the Hill method (Section 3.1), the proposed method employs appropriate mode tracking to discard spurious solutions.
- Resolution of Floquet exponent ambiguity. The method uniquely determines the imaginary part of the Floquet exponents. In Section 5, this is demonstrated by initializing the solver at hover conditions and progressively increasing the advance ratio to simulate forward flight.
- No computation of the monodromy matrix. Traditional methods require numerical integration of the monodromy matrix, which is highly sensitive to numerical precision (Maurice et al., 2009). This sensitivity impacts the accuracy of extracted Floquet exponents and increases computational costs for high-fidelity aerodynamic models. The proposed frequency-domain formulation eliminates this requirement.
- No need to define appropriate system perturbations. Unlike partial Floquet analyses when using high-fidelity aerodynamic models (Torok and Chopra, 1990; Bauchau and Wang, 2010; Skjoldan and Bauchau, 2011; Zaki, 2012), the proposed method does not require system perturbations. Instead, aeroelastic eigenmodes are tracked from hover conditions, analogous to wind-off tracking in time-invariant cases.
- Compatibility with high-fidelity aerodynamic models. The method supports aerodynamic models without requiring a statespace form, enabling direct incorporation of complex high-fidelity models or experimental data into stability analysis.

### 5. Application case

In this section, the stability characteristics of a two-dimensional airfoil with two degrees of freedom (heave h and pitch  $\alpha$ ) in a pulsating oncoming flow,  $U_{\infty}(t)$ , are considered. This configuration represents the cross-section of a helicopter rotor blade in forward flight. Fig. 5 illustrates the aerodynamic environment encountered by the rotor blade in this condition.

Various theories for predicting the lift and pitch moment of a moving airfoil in a varying freestream have been presented in van der Wall and Leishman (1994). Among these, only the arbitrary motion theory (AMT) allows for an arbitrary variation in both the freestream and the airfoil motion. This work adopts the AMT approach, which is based on the assumptions of potential and incompressible flow. The lift L and pitch moment at the elastic axis location M are composed of circulatory (c) and noncirculatory (c) components (Dinyavari and Friedmann, 1986; van der Wall and Leishman, 1994; Johnson, 2012):

$$L(t) = L_c(t) + L_{nc}(t),$$
 (42)

$$L_{c}(t) = \pi \rho_{\infty} U_{\infty}(t) \left[ w_{3/4}(t=0) \phi(s) + \int_{0}^{s} \frac{dw_{3/4}(\sigma)}{d\sigma} \phi(s-\sigma) d\sigma \right], \tag{43}$$

$$L_{nc}(t) = \pi \rho_{\infty} \left(\frac{c^2}{4}\right) \left[\frac{d^2 h}{dt^2}(t) + U_{\infty}(t)\frac{d\alpha}{dt}(t) + \frac{dU_{\infty}}{dt}(t)\alpha(t) - a\left(\frac{c}{2}\right)\frac{d^2\alpha}{dt^2}(t)\right],\tag{44}$$

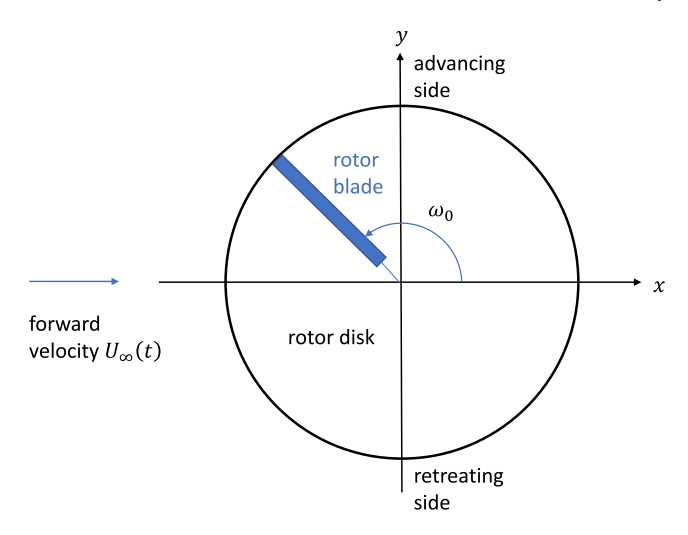


Fig. 5. Aerodynamic environment of the rotor in forward flight (Johnson, 2012).

Similarly, the pitch moment is expressed as:

$$M(t) = M_c(t) + M_{nc}(t),$$
 (45)

$$M_c(t) = \left(\frac{c}{2}\right)\left(a + \frac{1}{2}\right)L_c(t),\tag{46}$$

$$M_{nc}(t) = \pi \rho_{\infty} \left(\frac{c^3}{8}\right) \left[ \left(a - \frac{1}{2}\right) U_{\infty}(t) \frac{d\alpha}{dt}(t) + a \frac{d^2h}{dt^2}(t) + a \frac{dU_{\infty}}{dt}(t) \alpha(t) - \left(\frac{c}{2}\right) \left(\frac{1}{8} + a^2\right) \frac{d^2\alpha}{dt^2}(t) \right]. \tag{47}$$

In Eqs. (42) through (47), c represents the airfoil chord, while a is the elastic axis location normalized by the reference length  $L_{ref} = c/2$ . The variable h(t) denotes the arbitrary heave motion of the airfoil, and  $\alpha(t)$  represents the local pitch at the elastic axis. The Wagner function  $\phi(s)$ , which describes the lift response to a step change in the angle of attack, can be computed by the integral (Wagner, 1925; Jones, 1940; Tewari, 2015; Gülçat, 2021):

$$\phi(s) = \left(\frac{1}{2\pi}\right) \int_{-\infty}^{\infty} \frac{C(k)}{ik} e^{iks} dk = 1 + \left(\frac{2}{\pi}\right) \int_{0}^{\infty} \frac{\operatorname{Im}(C(k))}{k} \cos(ks) dk. \tag{48}$$

Here, C(k) is the Theodorsen function (Theodorsen, 1935), and Im denotes the imaginary part.

The varying freestream is denoted by  $U_{\infty}(t)$ . The nondimensional traveled distance s by the wake in the time-varying freestream is given by (Hansen et al., 2004):

$$s = \frac{2}{c} \int_0^t U_{\infty}(t) \, dt.$$

The formulation of AMT theory is based on the governing equations of linear, potential, and incompressible flow under a varying freestream  $U_{\infty}(t)$ , derived similarly to Theodorsen's approach. However, the wake vorticity  $\gamma_w$  is now considered as (Johnson, 2012):

$$\gamma_w = \gamma_w \left( \xi - \int_0^t U_\infty(t) dt \right),$$

where  $\xi$  is an integration variable along the direction of  $U_{\infty}\left(t\right)$ .

To facilitate the numerical implementation of the AMT theory, the integral in Eq. (43) is approximated using an expression for the Wagner function (Tewari, 2015):

$$\phi(s) = 1 - \sum_{i=1}^{n_a} A_j e^{-b_j s},\tag{49}$$

where  $n_a$  represents the number of aerodynamic finite states selected. Using Jones' approximation (Jones, 1940), the constants are given as:

$$A_1 = 0.165, A_2 = 0.335, b_1 = 0.0455, b_2 = 0.3.$$

This approach enables direct evaluation of the approximation function, eliminating the need to compute the integral in Eq. (48).

### 5.1. Aerodynamic state-space representation

Approximating the Wagner function using the expression in Eq. (49), which consists of a finite series of exponential terms, allows the aerodynamic model described by Eqs. (42) through (47) to be represented in a state-space formulation with time-dependent

coefficients, corresponding to a LTP system. Following the derivation of Hansen et al. (2004), the resulting state-space aerodynamic model is given by:

$$\frac{d}{dt} \begin{bmatrix} x_{a,1} \\ \vdots \\ x_{a,j} \\ \vdots \\ x_{a,n_a} \end{bmatrix} = \mathbf{A}_a(t) \begin{bmatrix} x_{a,1} \\ \vdots \\ x_{a,j} \\ \vdots \\ x_{a,n_a} \end{bmatrix} + \begin{bmatrix} \mathbf{B}_{a0}(t) & \mathbf{B}_{a1}(t) & \mathbf{B}_{a2}(t) \end{bmatrix} \begin{bmatrix} h \\ \alpha \\ \frac{dh}{dt} \\ \frac{dr}{dt} \\ \frac{d^2h}{dt^2} \\ \frac{d^2a}{dt^2} \end{bmatrix}, \tag{50}$$

which represents the state equation. The output equation, which provides the aerodynamic lift and pitch moment at the elastic axis, is given by:

$$\begin{bmatrix} L \\ M \end{bmatrix} = \mathbf{C}_{a}(t) \begin{bmatrix} x_{a,1} \\ \vdots \\ x_{a,j} \\ \vdots \\ x_{a,n_{a}} \end{bmatrix} + \begin{bmatrix} \mathbf{D}_{a0}(t) & \mathbf{D}_{a1}(t) & \mathbf{D}_{a2}(t) \end{bmatrix} \begin{bmatrix} h \\ \alpha \\ \frac{dh}{dt} \\ \frac{dt}{dt} \\ \frac{d^{2}h}{dt^{2}} \\ \frac{d^{2}h}{dt^{2}} \end{bmatrix}.$$

$$(51)$$

The periodic matrices  $\mathbf{A}_a(t)$ ,  $\mathbf{B}_{a0}(t)$ ,  $\mathbf{B}_{a1}(t)$ ,  $\mathbf{B}_{a2}(t)$ ,  $\mathbf{C}_a(t)$ ,  $\mathbf{D}_{a0}(t)$ ,  $\mathbf{D}_{a1}(t)$  and  $\mathbf{D}_{a2}(t)$  are provided in Appendix. The LTP system defined by Eqs. (50) and (51) corresponds to the state-space approximation of the AMT model described in Eqs. (42) through (47). For the general forward flight case with advance ratio u, the time-varying freestream velocity is given by (Johnson, 2012):

$$U_{\infty}(t) = \omega_0 R \left( 1 + \mu \sin \left( \omega_0 t \right) \right),$$

where  $\omega_0$  is the rotor angular speed. For the hover case ( $\mu=0$ ), the freestream velocity becomes constant,  $U_\infty=\omega_0 R$ , and the state-space system simplifies to a time-invariant form.

### 5.2. Aeroelastic system

In this section, the aeroelastic model is formulated in the time domain as an LTP system in state-space form. This formulation allows the application of either Floquet analysis or Hill's method to verify the results obtained from the frequency-domain flutter solver. The aeroelastic system in the time domain is described by Eq. (34).

For the specific case of a rotor blade section in incompressible potential flow, the aerodynamic forcing term is given by:

$$\mathbf{F}_{h} = \boldsymbol{\phi}_{gh}^{T} \begin{bmatrix} -L \\ M \end{bmatrix} = \boldsymbol{\phi}_{gh}^{T} \left( \mathbf{C}_{a} \mathbf{x}_{a} + \left[ \mathbf{D}_{a0} \ \mathbf{D}_{a1} \ \mathbf{D}_{a2} \right] \left[ \mathbf{u}_{h}^{T} \ \frac{d \mathbf{u}_{h}^{T}}{dt} \ \frac{d^{2} \mathbf{u}_{h}^{T}}{dt^{2}} \right]^{T} \right), \tag{52}$$

where the structural degrees of freedom are defined as  $\mathbf{u}_h = [h \ \alpha]^T$ . By substituting Eq. (52) into (34) and incorporating Eqs. (50) and (51), the state-space representation of the LTP aeroelastic system is obtained:

$$\frac{d}{dt} \begin{pmatrix} \mathbf{u}_h \\ \frac{d\mathbf{u}_h}{dt} \\ \mathbf{x}_a \end{pmatrix} = \mathbf{A}_{ae} (t) \begin{pmatrix} \mathbf{u}_h \\ \frac{d\mathbf{u}_h}{dt} \\ \mathbf{x}_a \end{pmatrix},$$
(53)

where the periodic state matrix  $A_{ae}(t)$  is provided in Appendix.

The stability of the aeroelastic system can be determined by extracting the eigenvalues of the monodromy matrix, as described in Section 2.1. Alternatively, stability can be assessed by solving the Hill determinant, as presented in Section 3.1, by computing the eigenvalues defined in Eq. (26).

### 5.3. Identification of the aerodynamic harmonic transfer function

In this section the aerodynamic GAF matrix is identified from time-domain simulations. By using the identified harmonic GAF, the frequency-domain flutter solver proposed in Section 4 can determine the aeroelastic eigenmodes and thus predict the stability of the aeroelastic system without requiring an explicit state-space representation of the aerodynamic system. The corresponding flutter stability analysis is presented in Section 5.4.

To identify the harmonic GAF, time-domain simulations are performed using a series of sine and cosine input signals imposed on each input component  $m = 1, ..., n_u$ , as described in Section 3.2. In this case, the number of inputs corresponds to the two degrees of freedom of the airfoil section: heave (h) and pitch  $(\alpha)$ . The outputs  $p = 1, ..., n_y$  correspond to the lift and moment at the elastic axis acting on the airfoil section and projected onto the structural modes by the matrix  $\phi_{vh}^T$ , yielding  $n_y = 2$ .

For time discretization, 192 equally spaced per period were chosen, and a total of seven periods were simulated, sufficient for transients to decay. For frequency discretization, values of  $\omega$  were distributed equally between 0 and 100 (rad/s) with a spacing

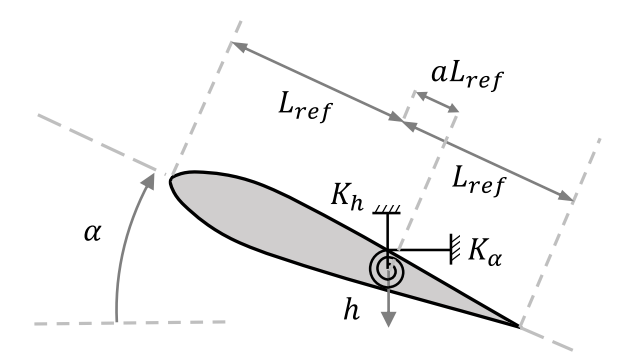
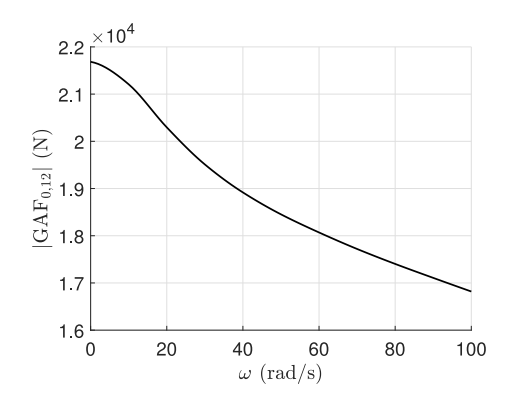


Fig. 6. Typical airfoil section with two degrees of freedom: heave (h) and pitch ( $\alpha$ ).



**Fig. 7.** Absolute value of the (1,2) component of the harmonic GAF matrix  $GAF_0(\omega)$ .

of 10 (rad/s). As noted in Eq. (24), due to the symmetry conditions of the HTF matrix, only positive frequency values need to be considered.

Fig. 6 illustrates the airfoil section. The distance between the elastic axis and the midchord point, nondimensionalized by the half-chord  $L_{ref}$ , is denoted as a. In the present application, the elastic axis is located at a = -1/2, with the reference length (half-chord) given by  $L_{ref} = c/2 = 0.209$  (m) (Laxman and Venkatesan, 2006). The fundamental frequency given by the rotor speed is  $\omega_0 = 22.82$  (rad/s), and the radial position R = 4.9518 (m).

Figs. 3 and 4 in Section 3.2 show typical time histories from the simulations at  $\omega=10$  (rad/s). The central column of the aerodynamic GAF matrix, see Eq. (31), is constructed by extracting the Fourier series coefficients from the last simulated period. The remaining columns are obtained by interpolating the values in the central column to  $\omega+in\omega_0$  for  $n=-n_H,\ldots,n_H$ . As noted earlier, for a harmonic GAF matrix containing  $n_H$  harmonics, twice the number of harmonics  $(2n_H)$  must be used in the Fourier series representation of the generated time-domain data.

Figs. 7 and 8 show the magnitude of the central column of a component of the harmonic GAF matrix (zeroth and first harmonics) for positive  $\omega$ . The values were computed with a frequency spacing of 10 (rad/s), but for the plotting purposes, a modified Akima interpolation (Akima, 1970) was applied separately to the real and imaginary. The same interpolation scheme is followed when solving the flutter equation in Section 5.4. In Fig. 7, the function GAF<sub>0</sub>( $\omega$ ) is presented, whereas in Fig. 8, GAF<sub>1</sub>( $\omega$ ) and GAF<sub>-1</sub>( $\omega$ ) are shown. A significant difference in magnitude is observed between GAF<sub>0</sub>( $\omega$ ) and the other components. Furthermore, due to the symmetry property given in Eq. (24), the relationship GAF<sub>n</sub>( $\omega$  = 0) = GAF̄<sub>-n</sub>( $\omega$  = 0) holds, meaning that at  $\omega$  = 0, they share the same absolute value.

### 5.4. Flutter stability analysis

In this section, the stability of the rotor blade section is analyzed for both in hover and forward flight across a range of advance ratio values  $\mu$ . The structural mass and stiffness matrices are defined in physical coordinates as:

$$\mathbf{M}_{gg} = \left[ \begin{array}{cc} m & S_{\alpha} \\ S_{\alpha} & I_{\alpha} \end{array} \right], \ \mathbf{K}_{gg} = \left[ \begin{array}{cc} K_{h} & 0 \\ 0 & K_{\alpha} \end{array} \right],$$

with the corresponding parameters structural parameters as given in Laxman and Venkatesan (2006) and  $S_{\alpha}=0$ :

$$m = 7.95$$
 (kg),  $I_a = 0.115$  (kg m<sup>2</sup>),  $K_h = 4396$  (N/m),  $K_a = 734.2$  (N m).

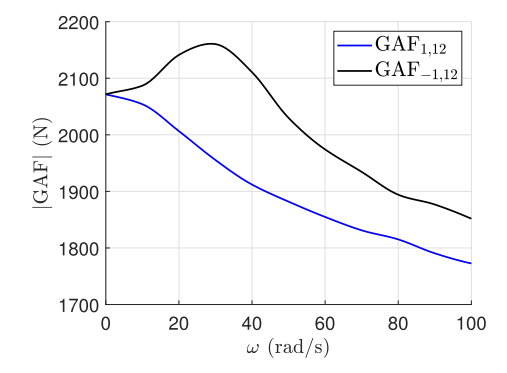


Fig. 8. Absolute value of the (1,2) component of the harmonic GAF matrices  $GAF_{-1}(\omega)$  and  $GAF_{-1}(\omega)$ .

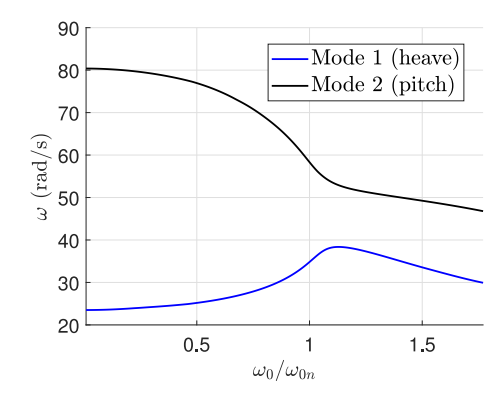


Fig. 9. Frequency of the aeroelastic eigenmodes as a function of the normalized rotor speed,  $\omega_0/\omega_{0u}$ .

For the selected application, the structural modes corresponding to the heave and pitch degrees of freedom of the rotor blade are independent of the rotor speed  $\omega_0$ . Consequently, the structural matrices  $\mathbf{M}_{hh}$  and  $\mathbf{K}_{hh}$  remain constant.

#### Hover

A stability analysis is first performed under hover conditions ( $\mu = 0$ ). In this case, the matrix  $\mathbf{A}_{ae}$  in Eq. (53) is time-independent, allowing stability to be determined using classical p-k or g methods. In this work, a nonlinear algebraic solver is used to obtain the aeroelastic eigenvalues and their corresponding eigenmodes.

A mode tracking technique is naturally implemented by selecting an initial value close to the expected aeroelastic eigensolution. Since the nonlinear solver requires an additional equation, one eigenmode component is set to 1. For further details, the reader is referred to Quero et al. (2021). The nonlinear solver is initialized with the structural eigenmodes  $\phi_{gh}$  at a low rotor speed,  $\omega_0/\omega_{0n}=0.01$ , with  $\omega_{0n}=22.82$  (rad/s) the nominal rotor speed. By progressively increasing the rotor speed, the evolution of the frequencies is shown in Fig. 9, as obtained using the g method, while the damping evolution is depicted in Fig. 10. At a normalized rotor speed of  $\omega_0/\omega_{0n}=1.3$  the system becomes unstable.

### Forward flight

The rotor speed is now set to the nominal value  $\omega_0 = \omega_{0n} = 22.82$  (rad/s), and the advance ratio  $\mu$  is incrementally increased from 0 (hover condition) to 0.8 in steps of 0.1.

Fig. 11 illustrates the evolution of the two aeroelastic eigenmodes in the complex plane for the h-g flutter solver using one harmonic ( $n_H$  = 1), along with a subset of the eigenvalues obtained from the Hill method by solving the eigenvalue problem defined in Eq. (26) for increasing  $\mu$ . From the plot, it is evident that the differences between the two methods become more pronounced for eigenvalues further from the imaginary axis. This occurs because the h-g flutter solver employs an approximation similar to the g method, which uses a first-order approximation for values outside the imaginary axis. The case of one harmonic is presented for illustrative purposes; however, for a higher number of harmonics, simple eigenvalue tracking is no longer sufficient, and a more sophisticated approach using periodic eigenmodes is required. A key observation from this plot is that the h-g method remains valid for aeroelastic eigenvalues closer to the imaginary axis, which are the most relevant for flutter onset prediction.

Next, the number of harmonics is increased to  $n_H=3$ . Fig. 12 shows the evolution of the most critical aeroelastic eigenvalue (the second mode, which corresponds mainly to the pitch degree of freedom in vacuum and hover) in the complex plane, as computed by four different methods: (1) the LTI averaging method described in Section 2.1; (2) the h-p-k method with three harmonics; (3)

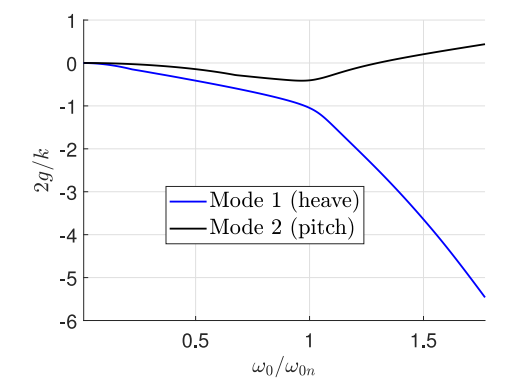


Fig. 10. Damping 2g/k of the aeroelastic eigenmodes as a function of the normalized rotor speed,  $\omega_0/\omega_{0w}$ .

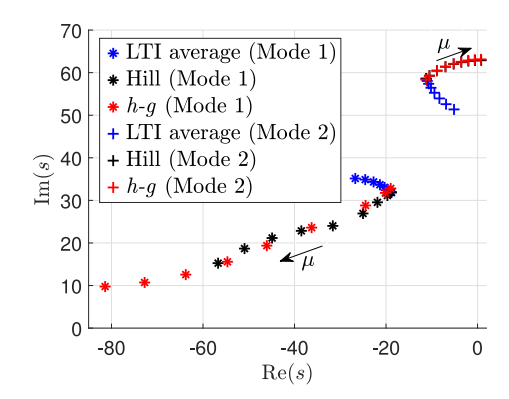


Fig. 11. Evolution of the two aeroelastic eigenmodes in the complex plane for a varying advance ratio  $\mu$ , as predicted by different methods  $(n_H = 1)$ .

the h-g method with three harmonics; and (4) the Floquet method. For the Floquet method, the monodromy matrix is obtained through numerical integration, as described in Section 2.1. The characteristic multipliers are computed from its eigenspectrum, and the Floquet exponents are obtained using Eq. (11). For the LTI average method, a straightforward eigenvalue computation provides the aeroelastic eigenmodes.

A notable observation from Fig. 12 is that all methods, except for the h-p-k, produce nearly identical results at hover ( $\mu = 0$ ). This discrepancy arises because the h-p-k method is not suitable for representing damping effects further from the imaginary axis. Additionally, a small discrepancy between the h-g flutter solver and the LTI average system arises due to the approximation of aerodynamic complex values from the imaginary axis. Furthermore, using the LTI average system would incorrectly suggest that the system remains stable at  $\mu = 0.8$ , whereas in reality, flutter occurs before this advance ratio value. The LTI method also fails to accurately describe the damping and frequency variations, as previously observed by Maier et al. (1999), Maurice et al. (2009) and Panda and Chopra (1985).

As described in Section 4, the h-p-k method, analogous to the p-k method used in fixed-wing aeroelastic analyses, loses accuracy as the Floquet exponents move further from the imaginary axis, as clearly demonstrated in Fig. 12. While the h-p-k solver provides satisfactory predictions for exponents near the imaginary axis, its accuracy diminishes with increasing damping. In contrast, the h-g flutter solver yields more reliable results under conditions of significant damping, highlighting its superiority for such cases. Most importantly, the evolution of the most critical aeroelastic eigenmode predicted by the h-g solver across the range of  $\mu$  values considered closely matches that obtained from the Floquet method, which is used as the reference solution. Notably, the results from the h-g flutter solver are obtained entirely in the frequency domain, eliminating the need for monodromy matrix computation.

Fig. 13 depicts the evolution of the most critical aeroelastic eigenvalue in the complex plane as the number of harmonics ( $n_H$ ) in the h-g flutter solver is progressively increased. The results obtained with  $n_H$  = 2 and  $n_H$  = 3 are nearly identical and align closely with the aeroelastic eigenvalue predicted by the Floquet analysis using the monodromy matrix in the time domain.

To further validate the h-g flutter solver, the stability analysis is repeated using the harmonic GAF matrix directly obtained from the aerodynamic LTP system in state-space form. Using Eqs. (50) and (51), the harmonic GAF matrix is computed for  $n_H = 3$  by solving a truncated version of Eq. (22) evaluated at the imaginary axis ( $s = i\omega$ ). To eliminate dependencies on the first and second time derivatives of the generalized coordinates, a low-pass filter is applied, as described in Appendix B of Quero (2024):  $n_0 = d_0 = \left(3\omega_{max}\right)^2$  and  $d_1 = 1.5\omega_{max}$ . The filtering parameter  $\omega_{max}$  has been set to the maximum structural frequency in wind-off conditions corresponding mainly to the pitch degree of freedom, given by  $\omega_{max} = 80.38$  (rad/s), as observed in Fig. 9 for

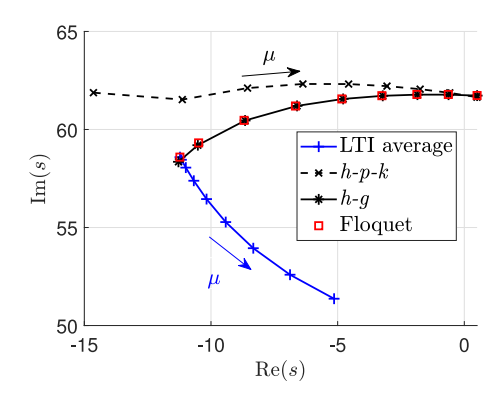


Fig. 12. Comparison of the critical aeroelastic eigenmode in the complex plane for a varying advance ratio  $\mu$ , as predicted by different methods ( $n_H = 3$ ).

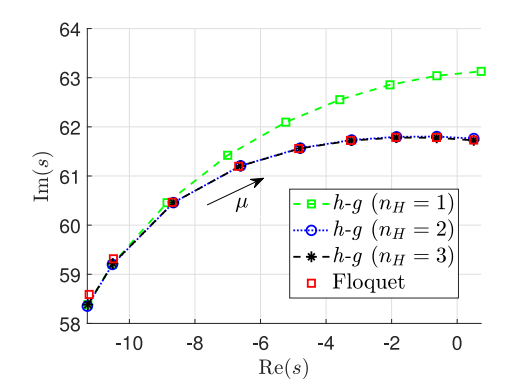


Fig. 13. Critical aeroelastic eigenmode in the complex plane for a varying advance ratio  $\mu$ , evaluated using the h-g flutter solver with different numbers of harmonics  $n_H$ .

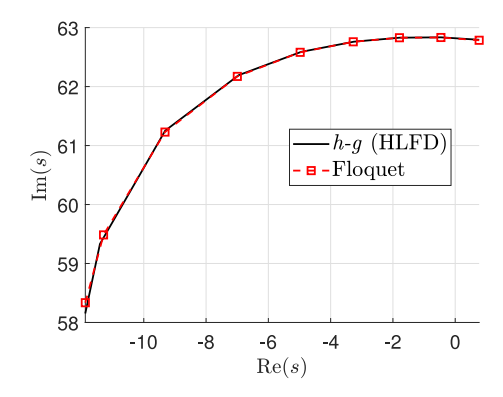


Fig. 14. Critical aeroelastic eigenmode in the complex plane for a varying advance ratio  $\mu$ , evaluated using the h-g flutter solver with different numbers of harmonics  $n_H$ . The harmonic GAF is computed entirely in the frequency domain.

zero rotor speed. Fig. 14 presents the evolution of the most critical aeroelastic eigenmode obtained by the *h-g* flutter solver with the harmonic GAF from Eq. (22), compared against the Floquet analysis. As expected, the results coincide, further validating the proposed approach. Differences relative to the results in Fig. 13 are due to the introduced low-pass filter.

The proposed flutter solution method introduces two novel approaches for computing the evolution of the aeroelastic eigenmode and predicting flutter onset, which were not previously available:

- · Computation entirely in the frequency domain: the harmonic GAF matrix is obtained from the Fourier series expansion of the state-space matrices.
- · Stability analysis without a known state-space aerodynamic model: as for the case when the output is derived by the convolution integral of Eq. (43), the harmonic GAF can be identified from specific input signals, as described in Section 3.2.

These two scenarios entirely bypass the need for the Floquet method, rendering it unnecessary for the stability analysis of LTP aeroelastic systems.

#### 6. Conclusions

This paper presents a novel frequency-domain flutter solver specifically designed for rotary-wing aeroelasticity, addressing the challenges associated with time-periodic aerodynamic forces, such as those experienced by helicopter rotor blades in forward flight. Unlike conventional methods based on Floquet theory, the proposed approach eliminates the need to construct a monodromy matrix, thereby reducing computational complexity and improving numerical stability.

The key contribution of this work is the introduction of harmonic extensions of the p-k and g flutter solvers, termed the h-p-k and h-g methods, respectively. By leveraging harmonic generalized aerodynamic forces, the method enables direct analysis of periodic aeroelastic systems without requiring a state-space formulation of the aerodynamic model. This flexibility allows for the integration of high-fidelity aerodynamic data and experimental results, making it a powerful tool for rotorcraft stability analysis.

The method was demonstrated on a two-degree-of-freedom rotor blade section in forward flight. The results validated that the frequency-domain flutter solver accurately predicts the flutter onset advance ratio and eigenmode stability trends, exhibiting strong agreement with Floquet-based solutions. Moreover, in the time-invariant case, the approach naturally reduces to the standard p-k and g solvers, confirming its robustness and consistency.

Beyond rotorcraft applications, the proposed frequency-domain method holds significant potential for extension to other linear time-periodic aeroelastic systems, including wind turbines and propellers operating under yawed conditions. Additionally, future research should focus on incorporating higher-fidelity aerodynamic models, as the flutter onset computation method presented is independent of the specific aerodynamic model employed. This adaptability ensures that the approach remains applicable across a wide range of aeroelastic configurations, further reinforcing its utility in stability analysis for periodic systems.

### Declaration of competing interest

The authors declare that they have no known competing financial interests or personal relationships that could have appeared to influence the work reported in this paper.

### **Appendix**

This appendix provides the periodic matrices of Eqs. (50) and (51) in Section 5.1. The periodic matrix  $A_a(t)$  is given by:

$$\mathbf{A}_{a}\left(t\right) = \begin{bmatrix} -\frac{b_{1}2U_{\infty}\left(t\right)}{c} & 0 & \cdots & 0\\ 0 & \ddots & & \vdots\\ \vdots & \cdots & -\frac{b_{j}2U_{\infty}\left(t\right)}{c} & \cdots\\ 0 & \cdots & & -\frac{b_{n_{a}}2U_{\infty}\left(t\right)}{c} \end{bmatrix}$$

The input matrices  $\mathbf{B}_{a0}(t)$ ,  $\mathbf{B}_{a1}(t)$  and  $\mathbf{B}_{a2}(t)$  are:

$$\mathbf{B}_{a0}\left(t\right) = \begin{bmatrix} 0 & \frac{b_{1}A_{1}U_{\infty}^{2}(t)}{c} \\ \vdots & \vdots \\ 0 & \frac{b_{j}A_{j}U_{\infty}^{2}(t)}{c} \\ \vdots & \vdots \\ 0 & \frac{b_{n_{a}}A_{n_{a}}U_{\infty}^{2}(t)}{c} \\ \vdots & \vdots \\ 0 & \frac{b_{n_{a}}A_{n_{a}}U_{\infty}^{2}(t)}{c} \end{bmatrix}, \quad \mathbf{B}_{a1}\left(t\right) = \begin{bmatrix} \frac{b_{1}A_{1}U_{\infty}(t)}{c} & \frac{b_{1}A_{1}(1-2a)U_{\infty}(t)}{4} \\ \vdots & \vdots \\ \frac{b_{j}A_{j}U_{\infty}(t)}{c} & \frac{b_{j}A_{j}(1-2a)U_{\infty}(t)}{4} \\ \vdots & \vdots \\ \frac{b_{n_{a}}A_{n_{a}}U_{\infty}(t)}{c} & \frac{b_{n_{a}}A_{n_{a}}(1-2a)U_{\infty}(t)}{4} \end{bmatrix}, \quad \mathbf{B}_{a2}\left(t\right) = \mathbf{0}.$$

The output matrices are

$$\mathbf{C}_{a}\left(t\right)=\pi\rho_{\infty}cU_{\infty}\left(t\right)\left[\begin{array}{ccc}1&0\\0&\left(\frac{c}{2}\right)\left(a+\frac{1}{2}\right)\end{array}\right]\left[\begin{array}{cccc}1&\cdots&1&\cdots&1\\1&\cdots&1&\cdots&1\end{array}\right],$$

$$\mathbf{D}_{a0}\left(t\right) = \pi \rho_{\infty} c \left[ \begin{array}{cc} 0 & U_{\infty}^{2}\left(t\right) A_{t} + \left(\frac{c}{4}\right) \frac{dU_{\infty}\left(t\right)}{dt} \\ 0 & \left(\frac{c}{2}\right) \left[\left(a + \frac{1}{2}\right) U_{\infty}^{2}\left(t\right) A_{t} + \left(\frac{c}{4}\right) a \frac{dU_{\infty}\left(t\right)}{dt} \right] \end{array} \right],$$

$$\mathbf{D}_{a1}(t) = \pi \rho_{\infty} c \begin{bmatrix} U_{\infty}(t) A_t & \left(\frac{c}{2}\right) U_{\infty}(t) \left[\left(1 - 2a\right) A_t + \frac{1}{2}\right] \\ \left(\frac{c}{2}\right) \left(a + \frac{1}{2}\right) U_{\infty}(t) A_t & \left(\frac{c^2}{4}\right) U_{\infty}(t) \left[\left(a + \frac{1}{2}\right) A_t + \frac{1}{2}\left(a - \frac{1}{2}\right)\right] \end{bmatrix},$$

$$\mathbf{D}_{a2}\left(t\right) = \pi \rho_{\infty} c \begin{bmatrix} \frac{c}{4} & -a\left(\frac{c^2}{8}\right) \\ \frac{ac^2}{8} & -\left(\frac{c^3}{16}\right)\left(\frac{1}{8} + a^2\right) \end{bmatrix},$$

where:

$$A_t = 1 - \sum_{i=1}^{n_a} A_a.$$

 $A_t = 1 - \sum_{j=1}^{n_a} A_a.$  The periodic matrices of Eq. (53) in Section 5.2 is:

$$\mathbf{A}_{ae}\left(t\right) = \left[ \begin{array}{ccc} \mathbf{0} & \mathbf{I}_{n_h} & \mathbf{0} \\ \alpha \left(\mathbf{D}_{a0} - \mathbf{K}_{hh}\right) & \alpha \left(\mathbf{D}_{a1} - \mathbf{B}_{hh}\right) & \alpha \left(\mathbf{D}_{a0} - \mathbf{K}_{hh}\right) \\ \mathbf{B}_{a0} + \mathbf{B}_{a2}\alpha \left(\mathbf{D}_{a0} - \mathbf{K}_{hh}\right) & \mathbf{B}_{a1} + \mathbf{B}_{a2}\alpha \left(\mathbf{D}_{a1} - \mathbf{B}_{hh}\right) & \mathbf{A}_a + \mathbf{B}_{a2}\alpha \mathbf{C}_a \end{array} \right]$$

where.

$$\alpha = \left(\mathbf{M}_{hh} - \mathbf{D}_{a2}\right)^{-1}.$$

### Data availability

Data will be made available on request.

#### References

Akima, H., 1970. A new method of interpolation and smooth curve fitting based on local procedures. J. ACM 17 (4), 589-602. http://dx.doi.org/10.1145/

Allen, M., 2009. Frequency-domain identification of linear time-periodic systems using LTI techniques. J. Comput. Nonlinear Dyn. 4 (4), http://dx.doi.org/10.

Bauchau, O., Wang, J., 2010. Efficient and robust approaches for rotorcraft stability analysis. J. Am. Helicopter Soc. 55 (3), 32006. http://dx.doi.org/10.4050/ JAHS.55.032006.

Biggers, J., 1974. Some approximations to the flapping stability of helicopter rotors. In: AHS/NASA-Ames Specialists' Meeting on RotorcraftDynamics. https: //ntrs.nasa.gov/api/citations/19740026381/downloads/19740026381.pdf. (Accessed March 2025).

Bir, G., 2008. Multi-blade coordinate transformation and its application to wind turbine analysis. In: 46th AIAA Aerospace Sciencs Meeting and Exhibit. Reno, NV, USA, http://dx.doi.org/10.2514/6.2008-1300.

Bittanti, S., Colaneri, P., 2009. Periodic Systems: Filtering and Control. Springer London.

Bottasso, C., Cacciola, S., 2015. Model-independent periodic stability analysis of wind turbines. Wind. Energy 18 (5), 865-887. http://dx.doi.org/10.1002/we.1735. Chen, P., 2000. Damping perturbation method for flutter solution: The g-method. AIAA J. 38 (9), 1519-1524. http://dx.doi.org/10.2514/2.1171.

Crimi, P., 1969. A method for analyzing the aeroelastic stability of a helicopter rotor in forward flight. In: NASA CR-1332. https://ntrs.nasa.gov/api/citations/ 19690025366/downloads/19690025366.pdf. (Accessed March 2025).

Crimi, P., 1973. Analysis of stall flutter of a helicopter rotor blade. In: NASA CR-2322. https://ntrs.nasa.gov/api/citations/19740005595/downloads/19740005595. pdf. (Accessed March 2025).

Dinyavari, M., 1985. Unsteady Aerodynamics in Time and Frequency Domains for Finite-Time Arbitrary Motion of Helicopter Rotor Blades in Hover and Forward Flight (Ph.D. thesis). University of California.

Dinyavari, M., Friedmann, P., 1986. Application of time-domain unsteady aerodynamics to rotary-wing aeroelasticity. AIAA J. 24 (9), http://dx.doi.org/10.2514/ 3.9459.

Floquet, G., 1883. Sur les équations différentielles linéaires à coefficients périodiques. Ann. Sci. l'École Norm. Supérieure 47-88. http://dx.doi.org/10.24033/ asens, 220.

Friedmann, P., 1986. Numerical methods for determining the stability and response of periodic systems with applications to helicopter rotor dynamics and

aeroelasticity. Comput. Math. Appl. 12 (1), 131-148. http://dx.doi.org/10.1016/0898-1221(86)90091-X. Friedmann, P., 2004. Rotary-wing aeroelasticity: Current status and future trends. AIAA J. 42 (10), 1953-1972. http://dx.doi.org/10.2514/1.9022.

Friedmann, P., Hammond, C., Woo, T., 1977. Efficient numerical treatment of periodic systems with application to stability problems. Internat. J. Numer. Methods Engrg. http://dx.doi.org/10.1002/nme.1620110708.

Gaonkar, G., Peters, D., 1980. Use of multiblade coordinates for helicopter flap-lag stability with dynamic inflow. J. Aircr. 17 (2), http://dx.doi.org/10.2514/3. 57881

Gülçat, Ü., 2021. Fundamentals of Modern Unsteady Aerodynamics. Springer Cham, http://dx.doi.org/10.1007/978-3-030-60777-7.

Hansen, M., Gaunaa, M., Madsen, H., 2004. A beddoes-leishman type dynamic stall model in state-space and indicial formulations, Risφ-R-1354, https://dx.doi.org/10.1009/10.10 //backend.orbit.dtu.dk/ws/portalfiles/portal/7711084/ris\_r\_1354.pdf. (Accessed March 2025).

Hassig, H., 1971. An approximate true damping solution of the flutter equation by determinant iteration. J. Aircr. 8 (11), 885-889. http://dx.doi.org/10.2514/

Hidir, E., Uyanik, I., Morgül, Ö., 2019. Harmonic transfer functions based controllers for linear time-periodic systems. Trans. Inst. Meas. Control 41 (8), 2171-2184. http://dx.doi.org/10.1177/0142331218778748.

Houbolt, J., Brooks, G., 1958. Differential equations of motion for combined flapwise bending, chordwise bending, and torsion of twisted nonuniform rotor blades. In: NACA Technical Note 3905. https://ntrs.nasa.gov/api/citations/19930092334/downloads/19930092334.pdf. (Accessed March 2025).

Johnson, W., 2012, Helicopter theory, In: Dover Books on Aeronaurical Engineering,

Jones, R., 1940. The unsteady lift of a wing of finite aspect ratio. In: NACA Report No. 681. https://ntrs.nasa.gov/api/citations/19930091758/downloads/ 19930091758.pdf. (Accessed March 2025).

Laxman, V., Venkatesan, C., 2006. Rotor blade dynamic stall model and its influence on airfoil response. In: 47th AIAA/ASME/ASCE/AHS/ASC Structures, Structural Dynamics, and Materials Conference. http://dx.doi.org/10.2514/6.2006-1866.

Lazarus, A., Thomas, O., 2010. A harmonic-based method for computing the stability of periodic solutions of dynamical systems. C. R. Méc. 338 (9), 510-517. http://dx.doi.org/10.1016/j.crme.2010.07.020.

- Lowis, O., 1963. The stability of rotor blade flapping motion at high tip speed ratios. In: Reports and Memoranda No. 3544. https://reports.aerade.cranfield.ac.uk/bitstream/handle/1826.2/2815/arc-rm-3544.pdf. (Accessed March 2025).
- Maggia, M., Eisa, S., Taha, H., 2020. On higher-order averaging of time-periodic systems: reconciliation of two averaging techniques. Nonlinear Dynam. 99, 813–836. http://dx.doi.org/10.1007/s11071-019-05085-4.
- Maier, T., Sharpe, D., Abrego, A., 1999. Aeroelastic stability for straight and swept-tip rotor blades in hover and forward flight. In: Proceedings of the 55th Annual Forum of the American Helicopter Society. Montreal, Canada, https://rotorcraft.arc.nasa.gov/Publications/files/Maier\_AHS99.pdf. (Accessed March 2025)
- Maurice, J., King, F., Fichter, W., Dieterich, O., Konstanzer, P., 2009. Floquet convergence analysis for periodic active rotor systems equipped with trailing edge flaps. In: 35th European Rotorcraft Forum. https://dspace-erf.nlr.nl/server/api/core/bitstreams/e0ca80a0-5777-40bf-9176-7b03dbbb4a6e/content. (Accessed March 2025).
- Möllerstedt, E., 2000. Dynamic Analysis of Harmonics in Electrical Systems (Ph.D. thesis). Lund Institute of Technology (LTH), https://lucris.lub.lu.se/ws/portalfiles/portal/4843151/8840250.pdf. (Accessed March 2025).
- Myklestad, N., 1944. A new method of calculating natural modes of uncoupled bending vibration of airplane wings and other types of beams. J. Aeronaut. Sci. 11 (2), 153–162. http://dx.doi.org/10.2514/8.11116.
- Ormiston, R., Warmbrodt, W.G., Hodges, D., Peters, D., 1988. Survey of army/NASA rotorcraft aeroleastic stability research. In: NASA Technical Memorandum 101026. https://ntrs.nasa.gov/api/citations/19890014958/downloads/19890014958.pdf. (Accessed March 2025).
- Panda, B., Chopra, I., 1985. Flap-lag-torsion stability in forward flight. J. Am. Helicopter Soc. 30 (4), 30-39. http://dx.doi.org/10.4050/JAHS.30.30.
- Peters, D., Hohenemser, K., 1971. Application of the floquet transition matrix to problems of lifting rotor stability. J. Am. Helicopter Soc. 16 (2), 25–33. http://dx.doi.org/10.4050/JAHS.16.25.
- Peters, D., Lieb, S., 2009. Significance of floquet eigenvalues and eigenvectors for the dynamics of time-varying systems. In: 65th Annual National Forum of the American Helicopter Society. Grapevine, Texas, https://vtol.org/store/product/significance-of-floquet-eigenvalues-and-eigenvectors-for-the-dynamics-of-timevarying-systems-2383.cfm. (Accessed March 2025).
- Peters, D., Su, A., 1990. The effect of hidden dynamic states on floquet eigenvalues. Am. Helicopter Soc. J. 35 (4), 72–75. http://dx.doi.org/10.4050/JAHS.35.72. Prohl, M., 1945. A general method for calculating critical speeds of flexible rotors. J. Appl. Mech. 12 (3), A142–A148. http://dx.doi.org/10.1115/1.4009455.
- Quero, D., 2024. Application of time-variant systems theory to the unsteady aerodynamics of rotary wings. AIAA J. 62 (10), http://dx.doi.org/10.2514/1.J064078.
- Quero, D., Vuillemin, P., Poussot-Vassal, C., 2021. A generalized eigenvalue solution to the flutter stability problem with true damping: The p-L method. J. Fluids Struct. 103, http://dx.doi.org/10.1016/j.jfluidstructs.2021.103266.
- Siddiqi, A., 2001. Identification of the Harmonic Transfer Functions of a Helicopter Rotor (Master thesis). Massachusetts Institute of Technology, https://dspace.mit.edu/bitstream/handle/1721.1/8900/48881143-MIT.pdf. (Accessed March 2025).
- Skjoldan, P., Bauchau, O., 2011. Determination of modal parameters in complex nonlinear systems. J. Comput. Nonlinear Dyn. 6 (3), http://dx.doi.org/10.1115/1.4002975.
- Skjoldan, P., Hansen, M., 2009. On the similarity of the Coleman and Lyapunov–Floquet transformations for modal analysis of bladed rotor structures. J. Sound Vib. 327 (3–5), 424–439. http://dx.doi.org/10.1016/j.jsv.2009.07.007.
- Stol, K., Moll, H., Bir, G., Namik, H., 2009. A comparison of multi-blade coordinate transformation and direct periodic techniques for wind turbine control design. In: 47th AIAA Aerospace Sciences Meeting. Orlando, FL, USA, http://dx.doi.org/10.2514/6.2009-479.
- Tewari, A., 2015. Aeroservoelasticity: Modeling and Control. Springer New York.
- Theodorsen, T., 1935. General theory of aerodynamic instability and the mechanism of flutter. In: NACA Technical Report 496. https://ntrs.nasa.gov/api/citations/19930090935/downloads/19930090935.pdf. (Accessed March 2025).
- Torok, M., Chopra, I., 1990. Hingeless rotor blade stability using a coupled aeroelastic analysis with refined aerodynamic modeling. In: American Helicopter Society, Annaul Forum, 46th. Washington D.C., https://vtol.org/store/product/hingeless-rotor-blade-stability-using-a-coupled-aeroelastic-analysis-with-refined-aerodynamic-modeling-1138.cfm. (Accessed March 2025).
- van der Wall, B., Leishman, J., 1994. On the influence of time-Varying flow velocity on unsteady aerodynamics. J. Am. Helicopter Soc. 39 (4), 25–36. http://dx.doi.org/10.4050/JAHS.39.25.
- Wagner, H., 1925. Über die Entstehung des dynamischen Auftriebes von Tragflügeln. J. Appl. Math. Mech. 5 (1), 17–35. http://dx.doi.org/10.1002/zamm.
- Wereley, N., 1991. Analysis and Control of Linear Periodically Time Varying Systems (Ph.D. thesis). Massachusetts Institute of Technology, https://dspace.mit.edu/bitstream/handle/1721.1/13761/24401077-MIT.pdf. (Accessed March 2025).
- Yeo, H., Potsdam, M., Ormiston, R., 2011. Rotor aeroelastic stability analysis using coupled computational fluid dynamics/computational structural dynamics. Vert. Flight Soc. 56 (4), 1–16. http://dx.doi.org/10.4050/JAHS.56.042003.
- Zadeh, L., 1950. Frequency analysis of variable networks. Proc. IRE 38 (3), http://dx.doi.org/10.1109/JRPROC.1950.231083.
- Zaki, A., 2012. Using Tightly-Coupled CFD/CSD Simulation for Rotorcraft Stability Analysis (Ph.D. thesis). Georgia Insitute of Technology, https://smartech.gatech.edu/bitstream/handle/1853/43579/zaki\_afifa\_a\_201205\_phd.pdf. (Accessed March 2025).